| Computational Biology | Observation

Single-cell ATAC sequencing identifies sleepy macrophages during reciprocity of cytokines in *L. major* infection

Shweta Khandibharad,[1] Shailza Singh[1]

AUTHOR AFFILIATION See affiliation list on p. 21.

ABSTRACT The hallmark characteristic of macrophages lies in their inherent plasticity, allowing them to adapt to dynamic microenvironments. *Leishmania* strategically modulates the phenotypic plasticity of macrophages, creating a favorable environment for intracellular survival and persistent infection through regulatory cytokine such as interleukin (IL)-10. Nevertheless, these effector cells can counteract infection by modulating crucial cytokines like IL-12 and key components involved in its production. Using sophisticated tool of single-cell assay for transposase accessible chromatin (ATAC) sequencing, we systematically examined the regulatory axis of IL-10 and IL-12 in a time-dependent manner during *Leishmania major* infection in macrophages Our analysis revealed the cellular heterogeneity post-infection with the regulators of IL-10 and IL-12, unveiling a reciprocal relationship between these cytokines. Notably, our significant findings highlighted the presence of sleepy macrophages and their pivotal role in mediating reciprocity between IL-10 and IL-12. To summarize, the roles of cytokine expression, transcription factors, cell cycle, and epigenetics of host cell machinery were vital in identification of sleepy macrophages, which is a transient state where transcription factors controlled the epigenetic remodeling and expression of genes involved in pro-inflammatory cytokine expression and recruitment of immune cells.

IMPORTANCE Leishmaniasis is an endemic affecting 99 countries and territories globally, as outlined in the 2022 World Health Organization report. The disease's severity is compounded by compromised host immune systems, emphasizing the pivotal role of the interplay between parasite and host immune factors in disease regulation. In instances of cutaneous leishmaniasis induced by *L. major*, macrophages function as sentinel cells. Our findings indicate that the plasticity and phenotype of macrophages can be modulated to express a cytokine profile involving IL-10 and IL-12, mediated by the regulation of transcription factors and their target genes post-*L. major* infection in macrophages. Employing sophisticated methodologies such as single-cell ATAC sequencing and computational genomics, we have identified a distinctive subset of macrophages termed "sleepy macrophages." These macrophages exhibit downregulated housekeeping genes while expressing a unique set of variable features. This data set constitutes a valuable resource for comprehending the intricate host-parasite interplay during *L. major* infection.

KEYWORDS single-cell ATAC sequencing, sleepy macrophages, parasite, systems biology, transcription factor

Effective immune functioning is influenced over the course of a lifetime by a niche of foreign entities through anthroponotic or zoonotic transfer. For combating these infections, immunological defense systems trigger phagocytosis or apoptosis, produce cytokines or antibodies, and release inflammatory or cytotoxic mediators (1). Nonetheless, the impact of infectious diseases is still substantial in low- and lower-middle-income

1

countries, and the mortality and morbidity attributable to neglected tropical diseases are also high (2), of which leishmaniasis is believed to have a high mortality rate in humans and is further correlated to the disadvantages of current medications, such as their high toxicity and drug resistance (3). Leishmaniasis is an intracellular protozoal infection that is chronic and is caused by multiple species of the genus *Leishmania*. Lines of evidence point toward leishmaniasis becoming more common due to factors like climate change, the discovery of effective vectors and reservoirs, a highly mobile population, significant population groups with documented exposure histories, HIV, and the widespread use of immunosuppressive drugs and organ transplants, encouraging potential for sustained autochthonous spread (4). Apart from standard drugs and Food and Drug Administration-approved drugs such as pentavalent antimonials, meglumine antimoniate, sodium stibogluconate, pentamidine, liposomal amphotericin B, and miltefosine, (3) novel therapeutic approaches are also progressing and gaining a lot of attention, such as phytotherapy, nanotherapeutics, metabolite encrichment, anti-microbial peptides, proteasomes, and epigenetic modifiers (5).

The chromatin remodeling in the parasite is thought to be significantly influenced by altered epigenetic histone modifications. It is intriguing to note that the parasite alters host gene expression as well, enabling the host immune response to be suppressed or hijacked. The silencing of genes specific to macrophages that are involved in defense against these parasites has been linked to epigenetic factors such DNA methylation of cytosine residues (6). Many studies highlight the potential of epigenetic factors as a prime target for vaccine as well as therapeutic target development. Recombinant histone H1 vaccination of monkeys resulted in a slower development of cutaneous lesions compared to controls, suggesting histone H1 can be a candidate for vaccine development against cutaneous leishmaniasis (CL) in humans (7). It was also reported that rLdH2-4 exclusively generates Thl-type immune responses, providing significant protection against experimental visceral leishmaniasis that cured patients/endemic contacts and hamsters (8). It was also shown that cutaneous lesions exhibit amplified matrix metalloproteinase 1, which may be regulated epigenetically by Friend leukemia virus integration 1 (FLI1) and interleukin (IL)-6, suggesting FLI1 can be a therapeutic target (9). Promising therapeutic targets might include the enzymes responsible for histone post-translational modifications, particularly those that contain epigenetic reader modules and bromodomains such as sirtuins of *Leishmania donovani* (6). The effect of imipramine on IL-10/IL-12 axis reciprocity was studied for clearance of antimony-resistant *L. donovani*, which specifically targeted host HDAC11, which inhibited its ability to acetylate IL-10 promoter region, leading to downregulation of IL-10 (10). Even though these vaccines and drugs with potentials to inhibit parasite growth have been reported, none of them has been introduced in the market specifically targeted toward any form of leishmaniasis. The shortcomings and limitations of these molecules are the phenotypic response of immune cells. In order to understand drug design, it is important to understand immune cell population as a network and dissecting the time-dependent response of the host immune cell toward parasite. Therefore, population dynamics, cell enrichment, phenotype characterization, and heterogeneity distribution may lay an insight as to which subsets of cells are playing a role in parasite proliferation and which genes are supporting the parasite survival process.

Majority of single-cell profiling investigations have so far relied on quantifying RNA by sequencing (single-cell RNA sequencing). While this offers glimpses of the intercellular and intracellular variations in gene expression, investigation into the epigenomic landscape in single cells has enormous promise for revealing a key component of the regulatory logic of gene expression programs (11). Together with the help of recent developments in array-based technologies, droplet microfluidics, and combinatorial indexing through split-pooling, the single-cell assay for transposase accessible chromatin using sequencing (scATAC-seq) has been able to generate chromatin accessibility data for thousands of single cells in a relatively simple and affordable way (11). Conventional methods that use bulk tissue samples as input lack the resolution to assess the temporal

dynamics of cell type-specific use. This methodology has been successfully implemented to embryonic tissues in *Drosophila melanogaster*, developing mouse forebrains, adult mouse tissues (12), human pancreatic islets (13), human testicular cells (14), fetal human retina (15), and mouse cardiac progenitor cells (16). This technique enables separation of cells by discriminating them on the basis of cell types, source, and cell variability to generate population clusters (17).

scATAC-seq is based on bulk ATAC-seq, which involves isolation of nuclei from single cells in the sample through fluorescence-activated cell sorter (FACS). Hyperactive Tn5 transposase catalyses the process of tagmentation by integrating sequencing adaptors to the targeted DNA by initiating its binding to the DNA followed by release from DNA post-tagging through heat or denaturing molecules. While nuclei are still intact, single nuclei are isolated (18). The nuclei are later lysed and loaded onto 96-well plates containing specially barcoded transposases, then sorted again before being dispensed into a second 96-well plate for FACS. Later, a second set of barcodes known as unique molecular identifiers are introduced in the amplification step (19). By identifying a distinct combination of both the barcode combinations, around 1,500 cells with a median range of 2,500 and 11% collision rate can be read (20). The downstream analysis may result in cell clustering that distinguishes between distinct cell types in a mixed cell population and find peaks that are more or less accessible to particular cell types (21), thus identifying complicated cell populations, connecting regulatory elements to their target genes, and mapping regulatory dynamics during complex cellular differentiation processes through the chromatin regulatory landscape on the cell clusters (13).

The ability of macrophages to phagocytose and promote parasite growth makes them prime resident cells for *Leishmania*, although these cells do function as the primary effector cells in the clearance of infection (22). Epigenetic modifications and chromatin remodeling framework of macrophages with respect to *L. major* infection that causes CL are still poorly understood. Macrophage being the most prime target of infection may dictate disease fate, and the modular characteristics of parasite may influence the host macrophage plasticity for survival (23). A fine balance exists between different types of macrophages such as pro-inflammatory cytokine-expressing macrophages which mediate Th1-type response and anti-inflammatory cytokine-expressing macrophages having different subsets such as M2a, M2b, M2c, and M2d that elevate Th2-type response which regulates the parasite clearance (24). As a component and regulator of adaptive immunity, macrophages facilitate expression of interferon gamma (IFN-γ) and tumor necrosis factor-alpha (TNF-α), IL-12 that facilitates production of nitric oxide. To endure the hostile macrophage environment, *Leishmania* subverts the macrophage cellular process and metabolic pathway molecular functions and promotes chromatin remodeling to produce immunosuppressive molecules such as transforming growth factor β and IL-10 for its survival (25). One of the key mechanisms of parasite survival which we had reported was through governing IL-10 and IL-12 reciprocity. Through computational and systems biology integrated framework models, we had previously reported that epigenetic factors such as NFAT5 and their regulators, mainly SHP-1, may play deterministic roles in regulating IL-10 and IL-12 reciprocity (26).

In this study, we elucidate the epigenetic framework and chromatin remodeling dynamics using single-cell ATAC sequencing of *L. major*-infected RAW264.7 mouse macrophage cell lines at various time points. We have identified regulatory motifs governing the reciprocal control of cytokines, the parasite's survival response, and infectivity. Our hypothesis posits that the observed shifts in population dynamics, cluster heterogeneity, and motif peak alterations are attributable to changes in the dynamic nature of chromatin accessibility. Additionally, we present, for the first time, quantified data at the single-cell level for macrophage-infected cells. *L. major* exhibits unique epigenetic modifications that are not reproduced by any other *Leishmania* spp. (27). Our previous findings had reported reciprocal expression of two crucial cytokines, IL-10 and IL-12, and we identified the time points of their distinct expression (26, 28). We introduce the term "sleepy macrophages" to characterize a subpopulation that does

not express housekeeping genes but exclusively expresses novel gene and transcription factors. We also propose that precision-targeted therapeutics could modulate phenotype populations and potentially contribute to disease resolution.

MATERIALS AND METHODS

Sample preparation

Four samples were submitted for sc-ATAC sequencing. Mouse derived stable macrophage cell line RAW264.7 cells (1×10^6) were infected with stationary-phase *L. major* promastigotes in 1:10 ratio and were incubated for 6, 12, and 18 h. Post-incubation, cells were washed thrice with phosphate-buffered saline (PBS) to remove unattached promastigotes, and cells were scrapped off and cryopreserved in cryomix [90% fetal bovine serum (FBS) + 10% dimethyl sulfoxide]; the control used for the study was uninfected RAW264.7 cells. To ensure maximum revival capacity of cells, they were frozen with gradual temperature changes: 0℃ for 30 min, −20℃ for 3 h, −80℃ overnight, and liquid nitrogen storage for 24 h. Each sample was submitted to Neuberg Centre for Genomic Medicine, Supratech Reference Laboratory, in duplicate for nuclei isolation, microfluidics-based library preparation, and sequencing.

Sample quality check

The cryovials were revived by thawing them at 37℃ in water bath for 2 min, followed by mixing with 10-mL pre-warmed media and centrifuged at 300 rcf for 5 min. The cell pellet was resuspended in 1× PBS + 0.04% bovine serum albumin (BSA) (Sigma #A2153) and passed through 40-µm Flowmi Cell Strainer (Sigma NB.01). To check the viability of cells post-revival, 20 µL of the sample and 20 µL of 0.4% trypan blue (ThermoFisher #15250061) were gently mixed; 10 µL of the mix was loaded into Countess cell counting chamber slides (Thermofisher #A51876). Cells were counted using Countess 3 FL Automated Cell Counter (ThermoFisher).

Nuclei isolation and quality check

Utilizing the CG000169 procedure from 10X Genomics, nuclei isolation was performed. The revived cells were centrifuged at 300 rcf for 5 min at 4℃. 100 µL lysis buffer containing 10 mM Tris-HCl (pH 7.4), 10 mM NaCl, 3 mM $MgCl_2$, 0.1% Tween 20, 0.1% Nonidet P40 substitute, 0.01% digitonin and 1% BSA was added and gently mixed 10 times, and the reaction mixture was incubated on ice for 5 min. To the lysed cells, 1-mL wash buffer [10 mM Tris-HCl (pH 7.4), 10 mM NaCl, 3 mM $MgCl_2$, 1% BSA, and 0.1% Tween-20] was added and mixed gently five times followed by centrifugation at 500 rcf for 5 min at 4℃. The supernatant was discarded and nuclei pellet was resuspended in 7 µL of chilled nuclei buffer. The fifth portion of 10-µL nuclei suspension buffer was made with nuclei suspension and nuclei buffer and was mixed with 10 µL of 0.4% trypan blue stain, of which 10 µL of the mix was loaded onto the slide chamber. Nuclei concentration and viability were quantified using Countess 3 FL Automated Cell Counter.

Transposition of isolated nuclei

Nuclei suspensions were incubated with transposase that was present in the transposition mix. Transposase fragments the DNA at open chromatin regions by entering the nuclei. Adapter sequences are simultaneously linked to the ends of the DNA fragments through polymerase chain reaction (PCR). The reaction mix was incubated at 50℃ for 30 min, 37℃ for 30 min, and 4℃ for hold.

Gel beads in emulsion and barcoding

Initiation of the steps was done by using CG000496 protocol. Briefly, barcoded gel beads, transposed nuclei, a master mix, and portioning oil loaded on a chromium Next

GEM Chip H were combined to achieve single-cell resolution using Chromium iX. The distribution of the nuclei occurred at a limiting dilution, such that most (90%–99%) of the resulting gel beads in emulsion (GEMs) had one or no nuclei, while the majority of the rest did. The gel beads dissolved following GEM synthesis. After mixing and releasing from (i) an Illumina P5 sequence, (ii) a 16-nucleotide 10× barcode, and (iii) a Read 1 (Read 1N), oligonucleotides were further taken for thermal cycling to generate 10× barcoded, single-stranded DNA. The samples for thermal cycler-based extension were incubated at 72°C for 5 min, 98°C for 30 s, 98°C for 10 s, 59°C for 30 s, and 72°C for 1 min; this cycle took place with 12 times repetition and finally was kept at 15°C to hold.

Single-cell library preparation and sequencing

During library preparation, P7 and a sample index wewere added through PCR. The P5 and P7 sequences used in Illumina bridge amplification were present in the final libraries. Following the manufacturer's instructions, final libraries were quantified using a Qubit v.4.0 fluorometer (ThermoFisher #Q33238) and a DNA HS test kit (ThermoFisher #Q32851). We scanned the library on the Tapestation 4150 (Agilent) using high-sensitive D1000 screentapes to determine the insert size. Final QC checked libraries were sequenced on Illumina (Novaseq 6000) using S Prime (SP) flowcell at 50:8:16:50 cycles. Post-sequencing, the data were demultiplexed using the cell ranger arc v.7.0, and BCL2FASTQs were futher processed to generate RAW FASTQ, websummary files and clope file using mm10 reference genome.

Clustering

Using log2 value as a filter parameter, custom filters were made to identify the population heterogeneity. We used Loupe browser for cell clustering. Peak calling is frequently repeated for each cluster in order to determine the accessible chromatin regions for various cellular populations. These regions are then the subject of a statistical test for correlations with different pre-defined genetic features. The primary objectives of downstream analysis techniques are to identify novel regulatory components and comprehend how they function within a cell (20).

Dimensionality reduction for identification of principal components

A key technique for examining scATAC-seq data sets is through principal component analysis (PCA). Reduction of data dimensions helps in big data processing, interpretation, and identifying the uniqueness of each component. We used Factoextra and FactoMineR to perform PCA. We considered the data table as X and transformed it to the original coordinate system by orthogonal linear transformation. Let Fs (or Gs) stand for the vector representing the coordinates for the rows (or columns) on the axis of rank *s*. According to the transition formulas, these two vectors are connected and represented as

$$Fs(i) = 1 \div \sqrt{\lambda s} \sum_k xikmkGs(k)$$
$$Gs(k) = 1 \div \sqrt{\lambda s} \sum_k xikpiFs(i)$$

where Fs(*i*) is the coordinate of individual *i* on axis *s*; Gs(*k*) is the coordinate of variable *k* on axis *s*; λs is the eigenvalue associated with axis *s*; mk is the weight assigned to variable *k*; pi is the weight assigned to individual *i*; and xik is the catchall concept of the data table (row *i*, column *k*) (29). As the 6-h infected sample showed presence of unique clusters, we identified the principal components (PCs) from the clusters of 6-h sample.

Gene set enrichment analysis

Gene set enrichment analysis (GSEA) enables evaluation of gene expression data at levels of gene sets, resolving the concerns arising due to insignificant statistics of

gene expression post-analysis, non-unique biological activity, identifying single gene function in cellular process, and preventing overlaps among phenotypes (30). Identification of gene sets to be involved with a specific biological activity, gene ontology, molecular function, or pathway, is compared to the ranked gene list. Determination of the enrichment score (ES), leading edge subset of genes, and gene rank was performed (31). We evaluated 814 genes from the 6-h sample in order to provide physiologically pertinent details regarding the differential expression of genes belonging to sleepy macrophages. The clusters were classified into two groups: sleepy macrophage (Clusters 3 and 6) and normal (Clusters 1, 2, 4, and 5) (Class 1 and 0, respectively), which were investigated for differential expression and enrichment.

Differential correlation analysis

It is critical to understand how the correlation between molecules under two different experimental conditions has changed, in addition to how the mean amounts of molecules in the omics data have changed. We employed DiffCorr package to understand the correlation among the clusters in the samples. For each data set, DiffCorr generates correlation matrices, locates the first principal component-based "eigen-molecules" in the correlation networks, and uses Fisher's z-test to assess differential correlations between the two groups (32). We performed differential correlation analysis for the 6-h sample.

Construction of transcription factor-target gene network

As the transcription factors which are expressed in Cluster 3 may result in upregulating the genes from the same cluster, we prepared an integrated framework network of the gene targets and transcription factors enriched in Cluster 3. We used the TFlink database, which offers thorough and extremely reliable information on transcription factor-target gene (TFTG) interactions for *Mus musculus*. It integrates information from other TF databases, including JASPAR and TRRUST database, to offer cumulative statistics for the TFs for a specific organism.

The entire integrated biomolecular interaction network of TFTG was constructed and analyzed using Cytoscape (v.3.6.0). The initial TFTG network had 814 genes obtained from Cluster 3 and 21 transcription factors. The constructed TFTG network consisted of 476 nodes and 1,060 edges. This initial network was then subjected to simulated annealing algorithm in Cytoscape, which will give a robust inter-regulatory TFTG network that is resilient and comprehensible in nature as the loosely connected edges of the network are filtered out. The most clustered or heavily weighted nodes are positioned at the bottom of the network using the simulated annealing process, which analyzes each node in the network. In contrast, nodes with lesser clusters are arranged in descending order in the upper part of the network.

The robust simulated annealing network obtained is further analyzed considering the potential of Cytoscape plugin: CytoHubba. CytoHubba uses a double screening scheme for ranking nodes and edges in a network. Further network analysis through CytoHubba helps us understand the function of an individual node and its collaboration with other nodes in a cluster. It uses algorithms like betweenness centrality, closeness centrality, degree of nodes, maximal clique centrality (MCC), clustering coefficient, bottleneck, and others to present a condensed and more robust nature of the inter-regulatory transcription factor network with their putative target genes.

Cell cycle analysis and effect on cell-cell communication

RAW264.7 cells were infected with stationary-phase *L.major* promastigotes for 6 h. They were washed thrice with PBS and fixed with 70% ethanol for 30 min at 4°C. Cells were later washed thrice with PBS to which RNase A (100 µg/mL, 0.1% Triton X and propidium iodide 50 µg/mL) was added and incubated for 15 min at room temperature (RT). Cells were acquired on BD New Canto II FACS analyzer.

By analysis of *k*-means of 6-h infection sample, we identified HOXA9 as the most statistically significant protein having the highest expression with a log2 fold change of 4.74. We identified the genes that are regulated by this protein and identified 7,241 genes. We mapped the ontologies associated with these genes using Consensus PathDB. Furthermore, we analyzed the expression of H2-D1 as it is the MHC-II associated with RAW264.7 cells. The log2 fold and motif accessibility were also investigated only to reveal the association of MHC-II with the cell cycle of the host.

Western blot analysis of peritoneal macrophages

Peritoneal macrophages were isolated from the peritoneal cavities of female (3–4 weeks old) Balb/c mice. Cells were adhered for 24 h in DMEM supplemented with 10% FBS and washed with PBS to remove non-adherent cells. Stationary-phase *L. major* promastigotes were used in 10:1 ratio to infect macrophages at different time points (1, 6, 12, 18, and 24 h). Further cells were scraped and washed with PBS thrice. Radioimmunoprecipitation assay buffer (RIPA) buffer was used to isolate protein from these samples. Protein estimation was done using bicinchoninic acid (BCA) assay. A total 20 µg of whole protein was loaded on 15% gel, which was further transferred on nitrocellulose membrane. The membrane was blocked with 3% BSA for an hour, which was later washed thrice with TBST. IL-10 [ThermoFisher Scientific (PA595561)] (1:1,000) and IL-12p40 [ThermoFisher Scientific (PA579461)] (1:1,000) primary antibodies were used for analysis. The blots were incubated for 18 h at 4°C. Following incubation, the blot was washed three times with TBST before being exposed to the secondary antibody, anti-rabbit IgG (whole molecule)-peroxidase antibody made in goat [Sigma-Aldrich (A9169)], which was incubated at room temperature for 1 h. Luminol-Enhancer Solution [Cyanagen (XLS070L)] and H_2O_2 [Cyanagen (XLS070P)] were used to develop the blot, and Amersham ImageQuant 800 imager was used to capture the images. Image J was used for densitometric analysis.

Confocal analysis of SHP-1 and NFAT5 at 6 h of infection

RAW264.7 cells was seeded on eight-well chamber slides. These were infected with stationary-phase *L. major* promastigotes for 6 h. Later, cells were washed with 1× PBST (PBS in 0.1% Triton X) and fixed with 4% paraformaldehyde for 20 min at RT. After washing the cells thrice with 1× PBST, the cells were permeabilized with 1× PBST for 10 min and blocked with 3% BSA for 30 min. SHP-1 [Cell Signaling Technology (3759S)] and NFAT5 [ThermoFisher Scientific (PA1-023)] primary antibodies were added to the cells and were incubated at RT for 2 h (1:1,000). Cells were washed thrice with PBST and later incubated with anti-rabbit IgG (H + L) F(ab′)2 fragment (AlexaFluor 488 Conjugate) [Cell Signaling Tachnology (4412S)] (1:500) and Mouse Phalloidin AlexaFluor 568 [ThermoFisher Scientific (A12380)] (1:500) for 1 h. Post-incubation, cells were washed with 1× PBST thrice and counterstained with 4′,6-diamidino-2-phenylindole (DAPI) for 10 min. Cells were later washed with 1× PBST thrice and with distilled water thrice. After air-drying the cells, mounting media [ThermoFisher Scientific (00-4958-02)] was used to mount the slides and were visualized at 60× and 100× on Zeiss LSM 880 with Airyscan microscope. Fiji was used for analysis of images.

RESULTS

Single-cell ATAC sequencing reveals diverse macrophage clusters post-*L. major* infection

A total of 2,262 cells were captured for uninfected cells, 1,886 cells from the 6-h infected sample, 10,835 cells from the 12-h infected sample, and 6,411 cells from the 18-h infected sample. Based on the log10 fragment value by depth, cells were clustered. Median high-quality fragments per cell for uninfected cells were 7,722; those for the 6-h infected cells were 32,590; those for the 12-h infected cells were 9,447; and those for the 18-h infected sample was 11,792 (Fig. S1).

After analysis of all the samples, 6 cell clusters were observed in the control and the 6-h sample, 12 clusters in the 12-h sample, and 10 clusters in the 18-h samples (Fig. S1 and S2). These clusters exhibited varying cell counts with diverse percentage distribution of macrophage population. There was an increase in the number of cell clusters from 6 to 12 h, although the number of cluster decreased at 18 h as compared to the 12-h sample. Also, the profiles of control and samples infected with *L. major* showed different clustering patterns, which differentiate infected and non-infected characteristics (Fig. S1 and S2).

Percentage population of pro-inflammatory cytokine and anti-inflammatory cytokine-expressing macrophages changes with time point of infection

Subtypes macrophages were identified based on their differential expression levels for which threshold for marker genes were set with cutoff log2 of >0.5. For identification of pro-inflammatory cytokine-expressing macrophages, we used IFN-γ and CD80 as markers as they may characterize parasite-eliminating response (24). Anti-inflammatory cytokine-producing macrophage subtypes commonly express IL-10; hence, to get an overview of parasite survival promoting response, we used IL-10 as a marker (24) for which threshold was set with a cutoff log2 of >0.5 (Fig. 1A1 through A4). Parasite-eliminating subsets are generally M2 subtypes, which include M2a, M2b, M2c, and M2d. These were characterized by expression of cell markers. Parameters for M2a were set as log2 CCl24 of >1 and log2 SOCS3 of >1; for M2b, log2 TNF of >1 and log2 CCl1 of >1; for M2c, log2 TGF-β of >1 and log2CD163 of >1; and for M2d, log2 NOS2 of>1 and log2 CCl5 of >1 (28) (Fig. S3). We could see the shift in macrophage population with time points of infection where IL-10-expressing macrophages and M2a population were most dominant
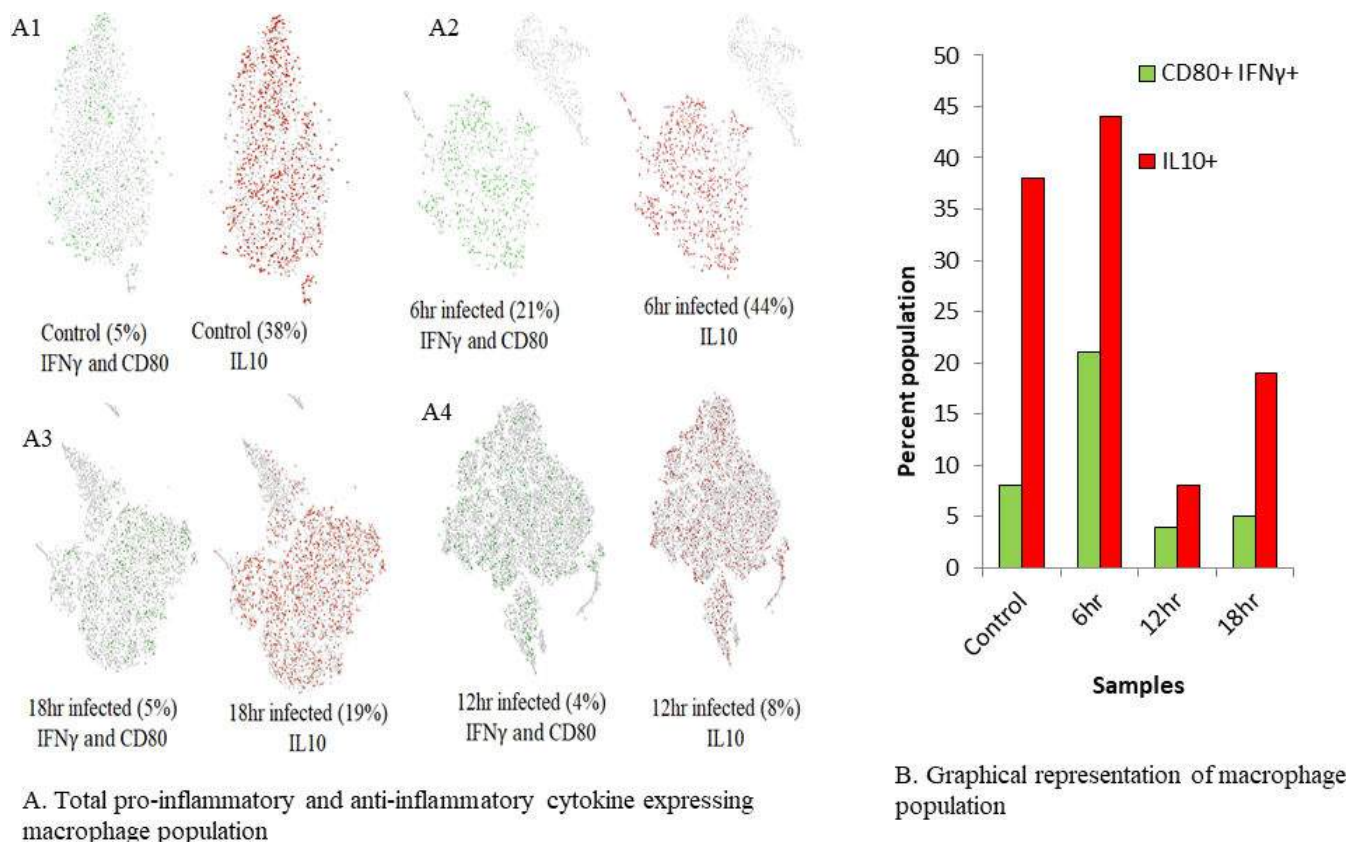

A. Total pro-inflammatory and anti-inflammatory cytokine expressing macrophage population

B. Graphical representation of macrophage population

FIG 1 (A) Expression of parasite eliminating phenotype and parasite survival promoting phenotype markers IFN-γ, CD80, and IL-10 in samples (CD80 IFN-γ -expressing cells are represented in green color and IL-10 -expressing cells in red). (A1) Control, (A2) 6 hr, (A3) 12 hr, and (A4) 18 h. (B) Graphical representation of macrophage types at different time points of infection.
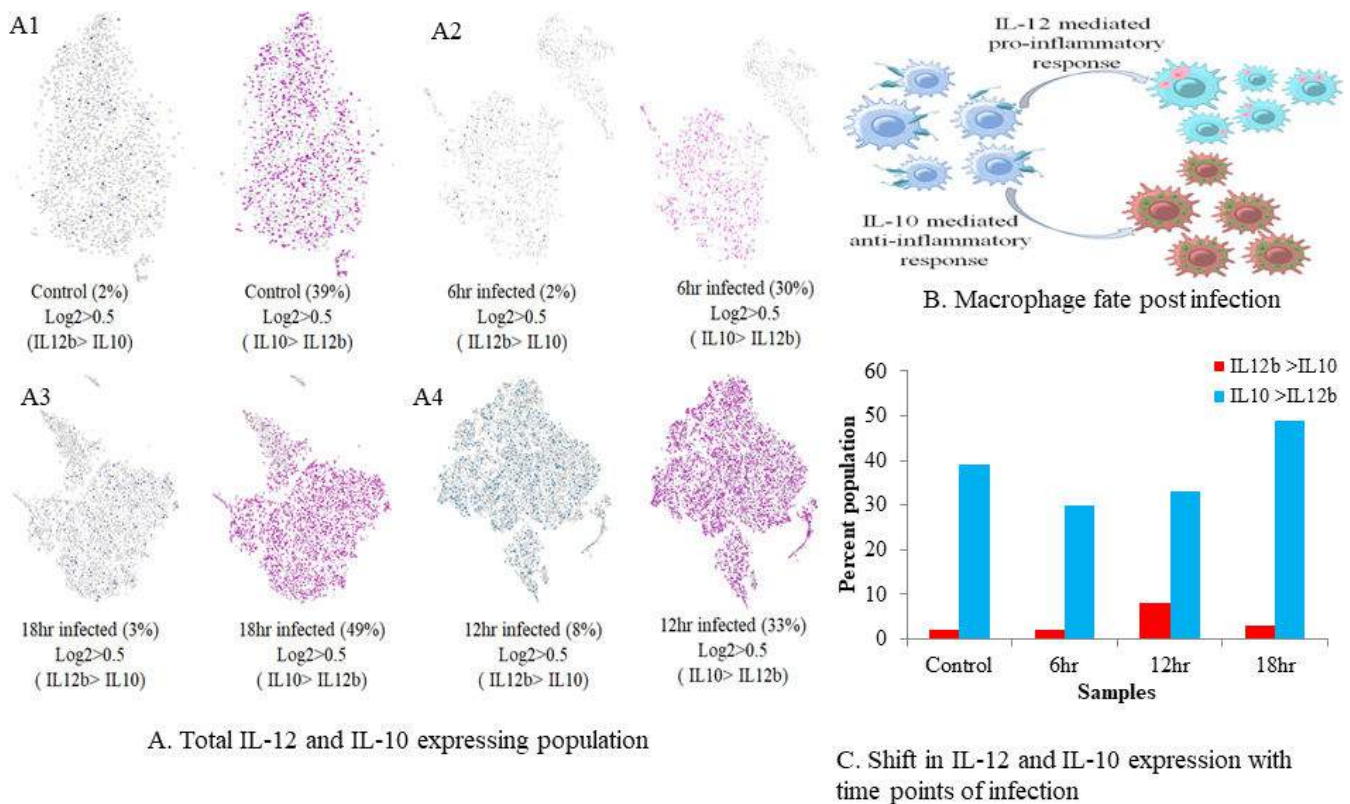
FIG 2 Identification of the reciprocal relationship between IL-10 and IL-12. (A) Macrophage-expressing IL-12 more than IL-10 and vice versa in all the samples. (A1) Control, (A2) 6 h, (A3) 12 h, and (A4) 18 h. (B) Abstract highlighting the fate of macrophages post-infection with *L. major* if IL-12 and IL-10 are secreted. (C) Change in expression patterns of IL-10 and IL-12 with time.

in all the samples; IFN-γ- and CD80-expressing population was most dominant in the 6-h infected sample; and M2d was enriched in the 6-h infected sample as well. In the 12-h infection sample, a decline in the number of cells was observed for all the macrophage types, which later at 18 h was followed by an increase in IL-10-expressing macrophage subtype (Fig. 1B; Fig. S3).

Infection of macrophages with *L. major* differentiates IL-10 and IL-12 production population

Macrophages may express IL-12, a pro-inflammatory cytokine, and IL-10, an anti-inflammatory cytokine, in response to *L. major* infection (Fig. 2B). Populations were identified based on unique expression of IL-12 or IL-10. This categorization identified the cellular response to infection with time. The parameter used was log2 IL-12b of >0.5 and log2 IL-10 of <0.5 for distinguishing the IL-12-producing group from the IL-10-producing group for which parameter for filtering was set as log2 IL-10 of >0.5 and log2 IL-12b of < 0.5 (Fig. 2A1 through A4). In the uninfected sample, we observed that populations expressing IL-10 were more than IL-12-expressing cells, although we observed slight changes in depletion of IL-10-producing cells at 6 h of infection. At 12 h, IL-12-expressing cells increased but did not dominate over IL-10-expressing cells, and they diminished at 18 h (Fig. 2C). We could deduce that perhaps, at 6 and 12 h post-infection, macrophages attempt to inhibit IL-10 production in favor of promoting IL-12 production. However, due to modulatory effects of intracellular *L. major* on regulation of host cytokine machinery, macrophages may fail to express IL-12 over IL-10, resulting in a subsequent decrease.

Reciprocal regulation of IL-10 and IL-12 through NFAT5 and SHP-1 expression

From our previous findings, we had already reported that upon *L. major* infection, NFAT5 might govern expression of IL-12 and nitric oxide. Furthermore, SHP-1 may regulate NFAT5 by dephosphorylating it at the auxiliary export domain. This inhibits the NFAT5-dependent pro-inflammatory response and steers the cellular machinery toward IL-10 and arginase-mediated ornithine cycle. (Fig. 3C). We identified if these deterministic genes are expressed together to get an insight into the IL-10 and IL-12 expression axis. Parameters used to identify these populations across samples were set as log2 NFAT5 motif of >0.5, log2 IL-12b sum of >0.5, and log2 NOS of >0.5. For the second group, the distinguishing parameters were set as log2 IL-10o of >0.5, log2 ptpn6 of >0.5, and log2 Arg1 of >0.5 (Fig. 3A1 through A4). We could discern that at 6 h of infection, the parasite-eliminating population was dominating over parasite survival-favoring population. At 12 h, population architecture dropped without changing the dynamics; however, at 18 h, the dynamics changed with subtle shift of parasite survival-favouring population over parasite-eliminating population (Fig. 3B).

Infection with *L. major* for 6 h identifies sleepy macrophages

As we observed the changes in gene expression pattern which shifted the cell population dynamics from parasite-eliminating group to parasite survival cell subset starting at 6 h post-infection, we analyzed the chromatin accessibility of IL-10, IL-12p40, SHP-1, and NFAT5 and used B-actin and GAPDH as housekeeping gene control. To our surprise, there were two clusters (Clusters 3 and 6) which showed minimal expression of housekeeping genes and genes under study (Fig. 4A through E) (Table 1). This made us intrigued as no other clusters from other samples
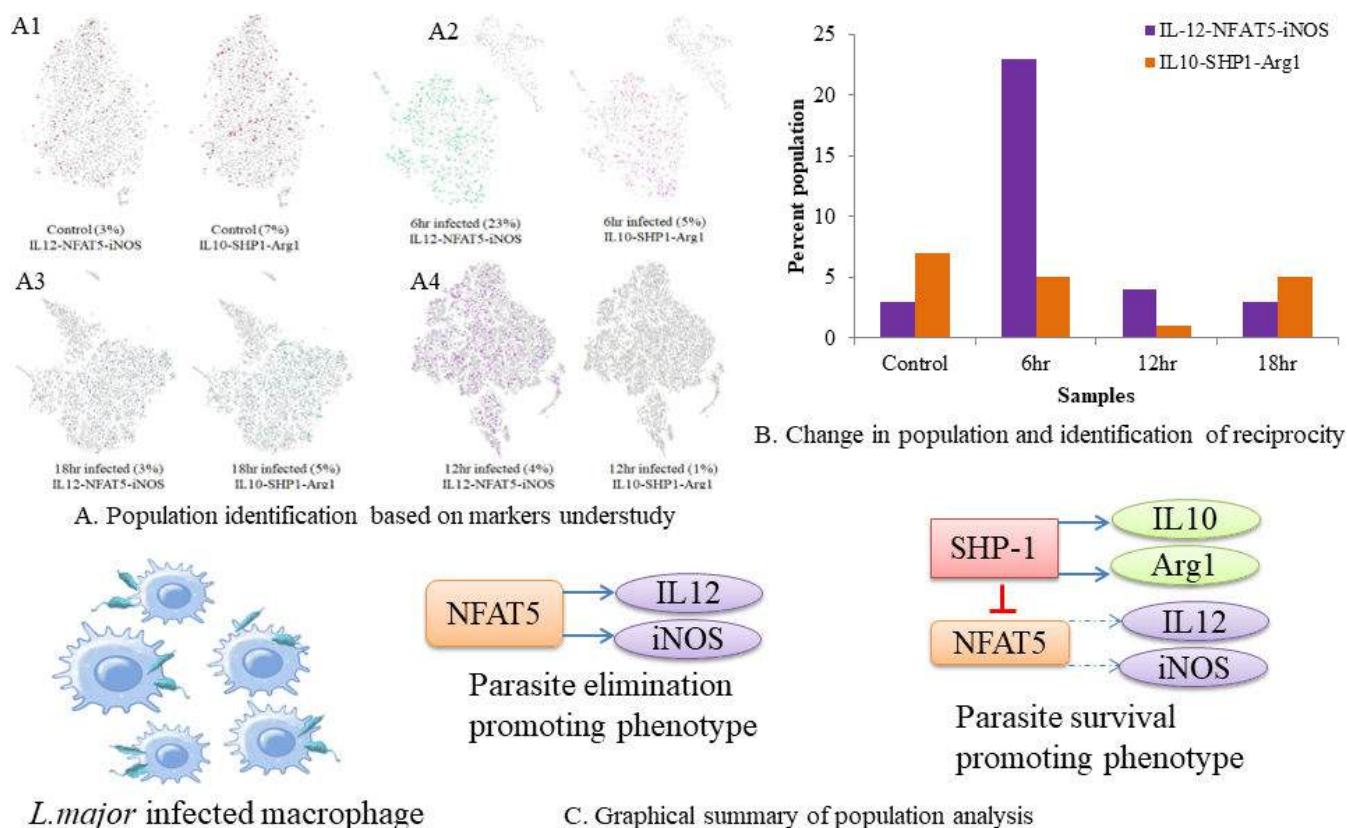

FIG 3 Identification of reciprocity in IL-10 and IL-12 expression patterns through NFAT5 and SHP-1. (A) Populations expressing IL-12, NFAT5, and iNOS versus populations expressing IL-10, SHP-1, and arginase1. (A1) Control, (A2) 6 h, (A3) 12 h, and (A4) 18 h. (B) Graphical representation highlighting the reciprocal relationship between IL-10 and IL-12 mediated by NFAT5 and SHP-1. (C) Graphical abstract of the aim behind the analysis.
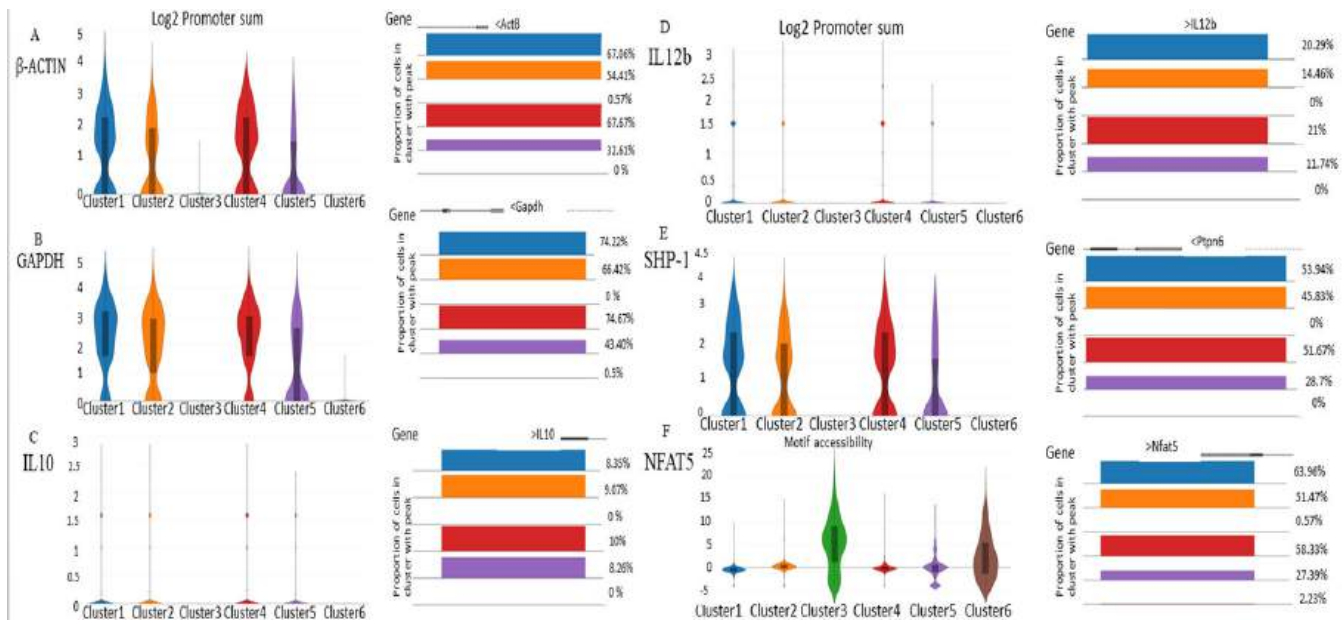
FIG 4 Differential expression of genes in 6-h sample in all clusters. (A) Violin plot of feature expression and peaks of ActB. (B) Violin plot of feature expression and peaks of GAPDH. (C) Violin plot of feature expression and peaks of IL-10 (D) Violin plot of feature expression and peaks of IL-12b. (E) Violin plot of feature expression and peaks of SHP-1. (F) Violin plot of NFAT5 motif accessibility and peak of NFAT5.

showed a similar expression pattern. These cells are alive; the chance that these undergo a survival mechanism in order to combat the infection was fascinating. As these macrophages were not expressing housekeeping genes, genes which we were studying, and any marker genes which macrophages normally express, we named them as sleepy macrophages to describe their dormancy. NFAT5 motif, which regulates IL-12 and IL-10 expressions, was highly enriched in sleepy macrophages (Fig. 4F), indicating potential involvement through molecular mechanisms, cellular processes, and biological signaling in sleepy macrophages to regulate the reciprocity of IL-10 and IL-12. Results for all samples are shown in Fig. S4.

Identification of principal components from sleepy macrophages

To discern the enriched genes in Clusters 3 and 6, we extracted the entire feature expression set from the 6-h sample. It was noted that the genes exhibiting upregulation in Clusters 3 and 6 are markedly downregulated in Clusters 1, 2, 4, and 5, as detailed in Table S1. The scree plot analysis disclosed an elbow point at Cluster 3, beyond which the slope became relatively flat. This observation indicates that variables from Clusters 4–6 exhibited low variance. Notably, Clusters 1–3 collectively account for 85.2% of

TABLE 1 Expression and accessibility of gene promoters under study

Gene	Median expression Cluster 3	Mean expression Cluster 3	Maximum expression Cluster 3	Percent peak range Cluster 3	Median expression Cluster 6	Mean expression Cluster 6	Maximum expression Cluster 6	Percent peak range Cluster 6
B-actin promoter sum	0	0.0090	1.58	0.571429	0	0	0	0
GAPDH promoter sum	0	0	0	0	0	0.00885	1.58	0.558659
IL-10 promoter sum	0	0	0	0	0	0	0	0
IL-12 promoter sum	0	0	0	0	0	0	0	0
SHP-1 promoter sum	0	0	0	0	0	0	0	0
NFAT5 promoter sum	0	0.00905	1.584	0.571429	0	0.0354	1.584	2.234637
NFAT5 motif	5.682141	5.28775	22.22298	N/A	1.745482	2.316064	18.40887	N/A

crucial variables, suggesting their suitability for further investigation to identify principal components, as illustrated in Fig. 5A. As a set of variables, Cluster 3 is observed in the negative quadrant, indicating that features from Cluster 3 may exhibit a negative correlation with variables from other clusters. (Fig. 5B). When individual genes were analyzed as eigenvectors, Cluster 3 displayed higher cos2 values in the positive quadrant (Fig. 5C). The significance of individual features as principal components is determined by the magnitude of their cos2 values; a higher cos2 value signifies greater importance. Subsequently, we identified principal components based on their level of significance from all the clusters (Table S3). PCs within the ellipses are notably contributing to the infection at 6 h, given the elevated number of highly significant principal components, as depicted in Fig. 5D, we proceeded to categorize the clusters for gene set enrichment. This approach aimed to identify potential components within crucial clusters that may play a regulatory role in the infection post-6 h of infection.

Gene set enrichment and differential correlation of sleepy macrophages

A heat map is employed to illustrate the expression of clustered genes within leading-edge subgroups. The correlation between ranked genes and the assigned class is visually represented on a heat map for each phenotype. In this instance, the heat map reveals that Clusters 3 and 6 exhibit elevated expression of the leading-edge subset of genes, indicating a correlation with the sleepy macrophage phenotype when compared to other clusters in the data set (Fig. 6A). In the enrichment plot, the magnitude of the increment in the enrichment plot depends on how well the gene correlates with the defined phenotype; the graph illustrates the positive enrichment of gene sets from Cluster 3 with an ES of greater than 0.8. Additionally, it was observed that the leading-edge subset of a gene set contributed to the sleepy macrophage phenotype as they
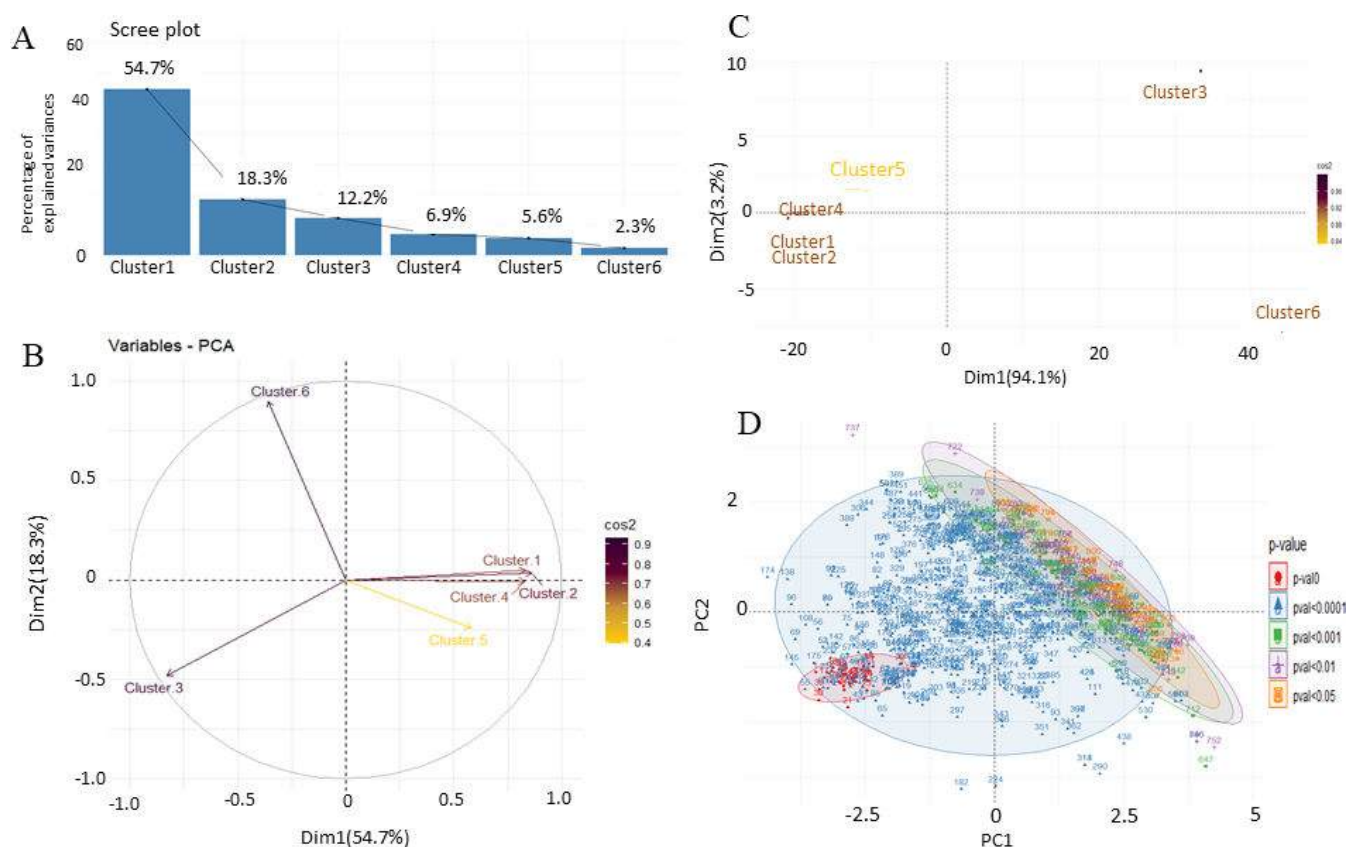

FIG 5 Principal component analysis of 6-h sample by differential expression of all the clusters. (A) Scree plot, (B) variables in clusters, (C) PCA of clusters, and (D) PCA based on *P* value.
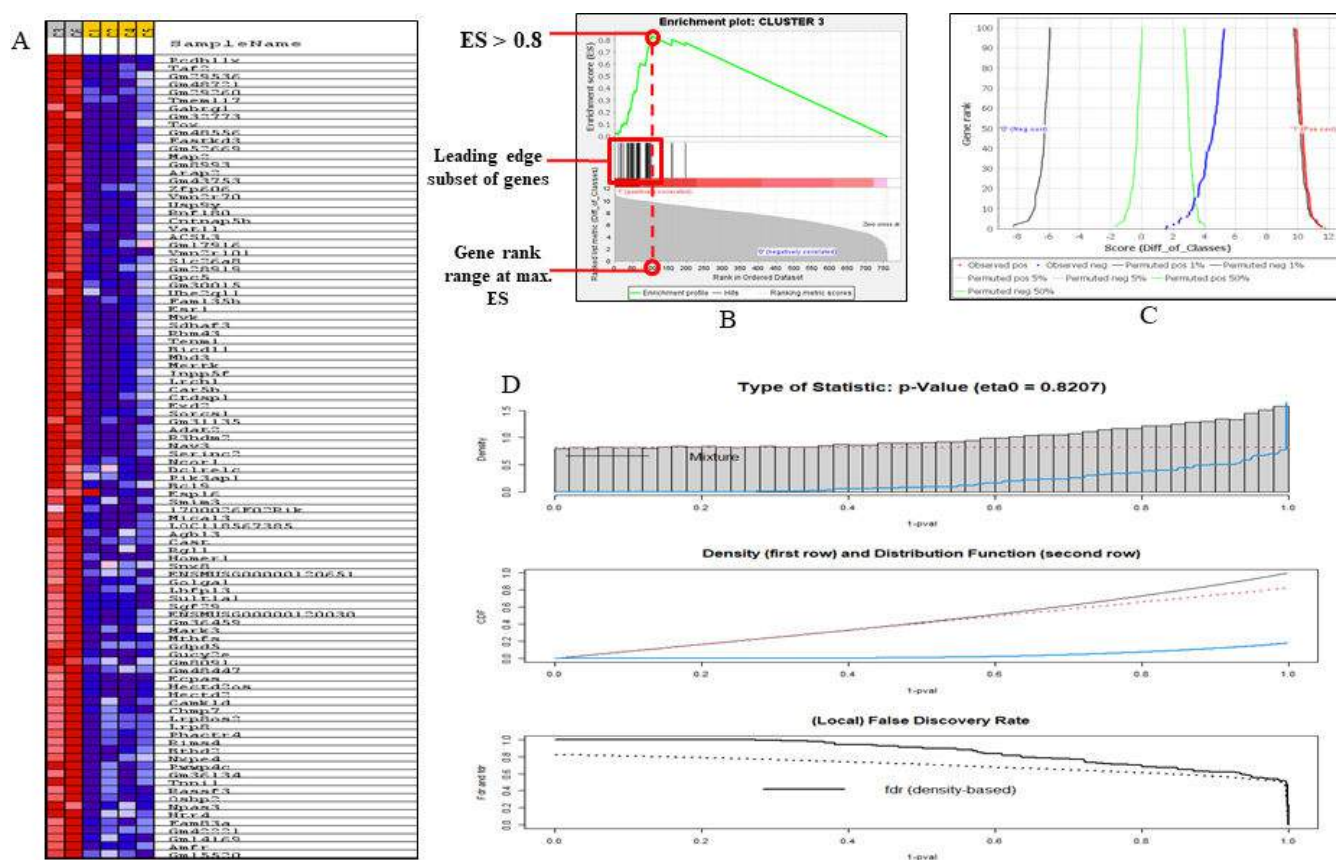
FIG 6 Gene enrichment analysis from Clusters 3 and 6 of 6-h sample. (A) Heat map of genes enriched from Clusters 3 and 6. The heat map visually displays the genes within the leading edge subsets after clustering. In this representation, gene expression values are depicted using a color spectrum where the variation in colors (ranging from red to pink, light blue to dark blue) corresponds to the diversity in expression levels (high, moderate, low, and lowest). (B) Enrichment plot of Cluster 3. (C) Butterfly plot of Cluster 3. (D) Differential correlation of Clusters 3 and 6 with Clusters 1, 2, 4, and 5.

were correspondingly located in the area under the ES plot. Furthermore, the bottommost portion of the enrichment plot shows the value of the ranking metric which measures every gene's correlation in the gene set with the defined phenotype. The ranking metrics' value goes from positive to negative as we move down the ranked list, with a positive value indicating correlation with the first phenotype sleepy macrophage and a negative value indicating correlation with the second phenotype (normal). With respect to the ES, the highest-ranking genes from the gene set fall between ranks 0 and 100 (Fig. 6B).

The butterfly plot provides a means to visually represent how permutations of the data set impact the correlation between gene ranking and the score assigned by the ranking metric. The observed correlation for the top genes, as well as permuted (1%, 5%, and 50%) positive and negative correlations, was calculated for the data set. The plot illustrates that 100 genes associated with the normal phenotype exhibit a negative correlation to sleepy macrophage, and the top-ranked genes shift more toward the sleepy macrophage phenotype, thereby providing support for the enrichment plots (Fig. 6C). Moreover, to observe the differential correlation pattern change in gene expression between Clusters 1, 2, 4, and 5 and Clusters 3 and 6, we performed (Table S7) differential correlation analysis using Pearson's correlation coefficient and observed density (P value) and distribution function to be correlated, with false discovery rate to be decreasing with P value (Fig. 6D).

TABLE 2 Statistical analysis of transcription factor-target gene inter-regulatory network after simulated annealing representing a decrease in the multi-edge node pairs, making the network more robust by filtering out the loosely connected edges

Parameters	Original network values	Simulated annealing network values
Clustering coefficient	0.005	0.005
Connected components	1	1
Network diameter	8	8
Network radius	4	4
Shortest paths	226,100 (100%)	226,100 (100%)
Characteristic path lengths	3.556	3.556
Average number of neighbors	4.454	4.454
Number of nodes	476	476
Network density	0.009	0.009
Isolated nodes	0	0
Number of self-loops	0	0
Multi-edge node pairs	16	0

TFTG network links cellular pathways and novel markers in sleepy macrophages

Our comprehensive study identified 51 transcription factors enriched in sleepy macrophages which may regulate 814 identified genes (Table S2); we could map 22 transcription factors and their target genes from sleepy macrophages genes and constructed the network, which had 476 nodes and 1,060 edges (see Fig. 8B and C; Table S6). The network was simulated in cytoscape as well as in simulated annealing algorithm environment. The network distribution was made lucid by reducing the number of multi-edge node pairs and weakly connected edges, making the network more robust (Table 2).

The significant transcription factors in the inter-regulatory TFTG network were identified using the Cytoscape plugin, CytoHubba. It was used to find the most essential modules and top 10 ranked nodes in the entire network. The 12 scoring methods used by CytoHubba to determine the critical network modules and top-ranked TFs/TGs in the inter-regulatory network include betweenness centrality, bottleneck, closeness centrality, clustering coefficient, degree centrality, eccentricity, edge percolating coefficient, MCC, density of maximum neighborhood component, maximum neighborhood component, radiality, and stress centrality (Fig. 7). The top 10 nodes in the network were determined by their frequency of occurrence in each scoring method, respectively. Mef2c, Isl1, Fosl2, Rxra, Jun, Pparg, Ascl1, Onecut2, and Gata1 were observed to be significantly enriched, out of which Mef2c and Isl1 were the two most critical transcription factors having the highest frequency of occurrence in the *L. major* infection (Fig. 8D). The ontologies associated with the top 10 transcription factors highlighted upregulation of NFAT5-mediated signaling, Th1 and Th2 cell differentiation, and histone deacetylase (HDAC)-mediated mitogen-activated protein kinase (MAPK) signaling (Fig. 8A).

Cell cycle arrest mediated by TP53 regulation interferes with MHC-II expression in sleepy macrophages

Cell cycle analysis of 6h infected sample identified 18.86% of cells in the G0/G1 phase, 2.53% of cells in the S phase, 1.11% of cells in the G2/M phase, and 76.88% of cells in the sub-G1 phase (Fig. 9A). *k*-Means analysis identified 51 genes which regulate sleepy macrophages, and they were associated with gene transcription and sumoylation (data not shown). Additionally, we aimed to investigate whether sleepy macrophages could engage in cell-cell communication through Signal 1, which is MHC-II and TCR/BCR interactions. We observed that H2-D1 allotype, which is expressed in the RAW264.7 cell
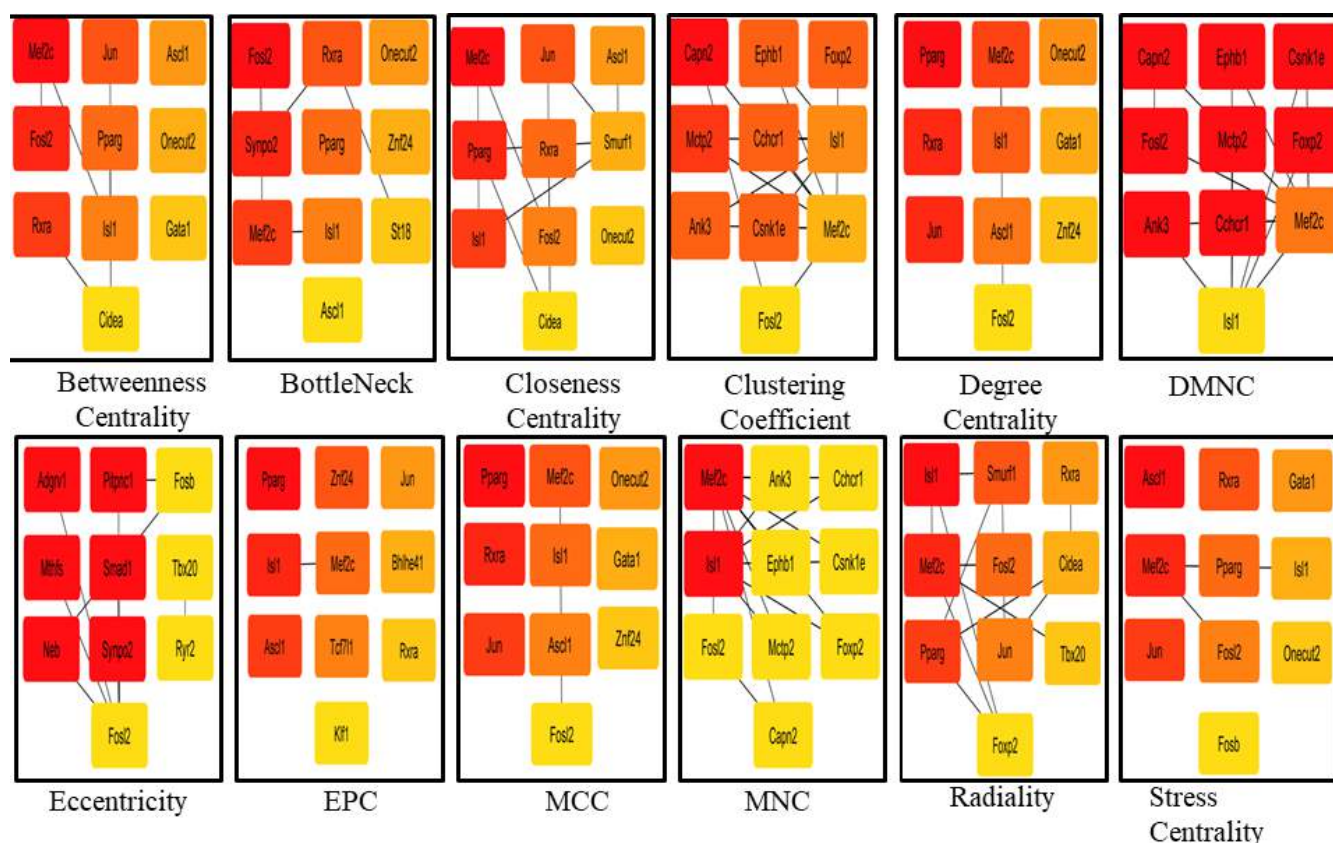
FIG 7 Top-ranking genes based on 12 scoring techniques were identified from the leading inter-regulatory TFTG network. Red signifies the highest score; orange signifies moderate score; and yellow signifies lower score.

line, was downregulated in sleepy macrophages, suggesting a silent defense mechanism of parasites which may deform host antigen processing mechanisms in order to process pathogen-associated molecular pattern molecules (PAMPs) of pathogen to activate other immune cells toward Th1 response (Fig. 9B and C). Furthermore, to see the connections associated with regulation of MHC-II expression, we analyzed the genes according to *k*-means and identified that TP53 regulation-mediated G1 and G2 arrest is prevalent in sleepy macrophages (Fig. 9E). The expression of TP53 was irregular in sleepy macrophages (Fig. 9F). When we analyzed the genes correlated with HOXA9, which was most abundantly and significantly expressed in sleepy macrophages, we found that TLR-mediated MyD88 pathway, cell cycle genes, cell cycle-associated genes, and TP53 expression and regulation were highly associated with sleepy macrophages (Fig. 9D).

Expression of NFAT5 and SHP-1 post-6-h infection with *L. major*

Expression of IL-10 and IL-12 was observed to have undergone alterations with time. Post-6 h, IL-12 levels had increased with even more higher expression of IL-10, and at 12 h, we observed that expression of both proteins had reduced followed by a shift in dynamicity where IL-10 expression had increased. Data from immunoblotting of peritoneal macrophages show similarity to the trend of expression in sc-ATAC time points, which was deciphered from RAW264.7 cells (Fig. 3A, B, 10A and B;Table S8). Localized expression of NFAT5 and SHP-1 at 6 h post-infection was significantly higher as compared to the uninfected sample, where NFAT5 expression at 6 h post-infection was highest as compared to other groups (Fig. 10C and D) and which also corroborates with (Fig. 4).
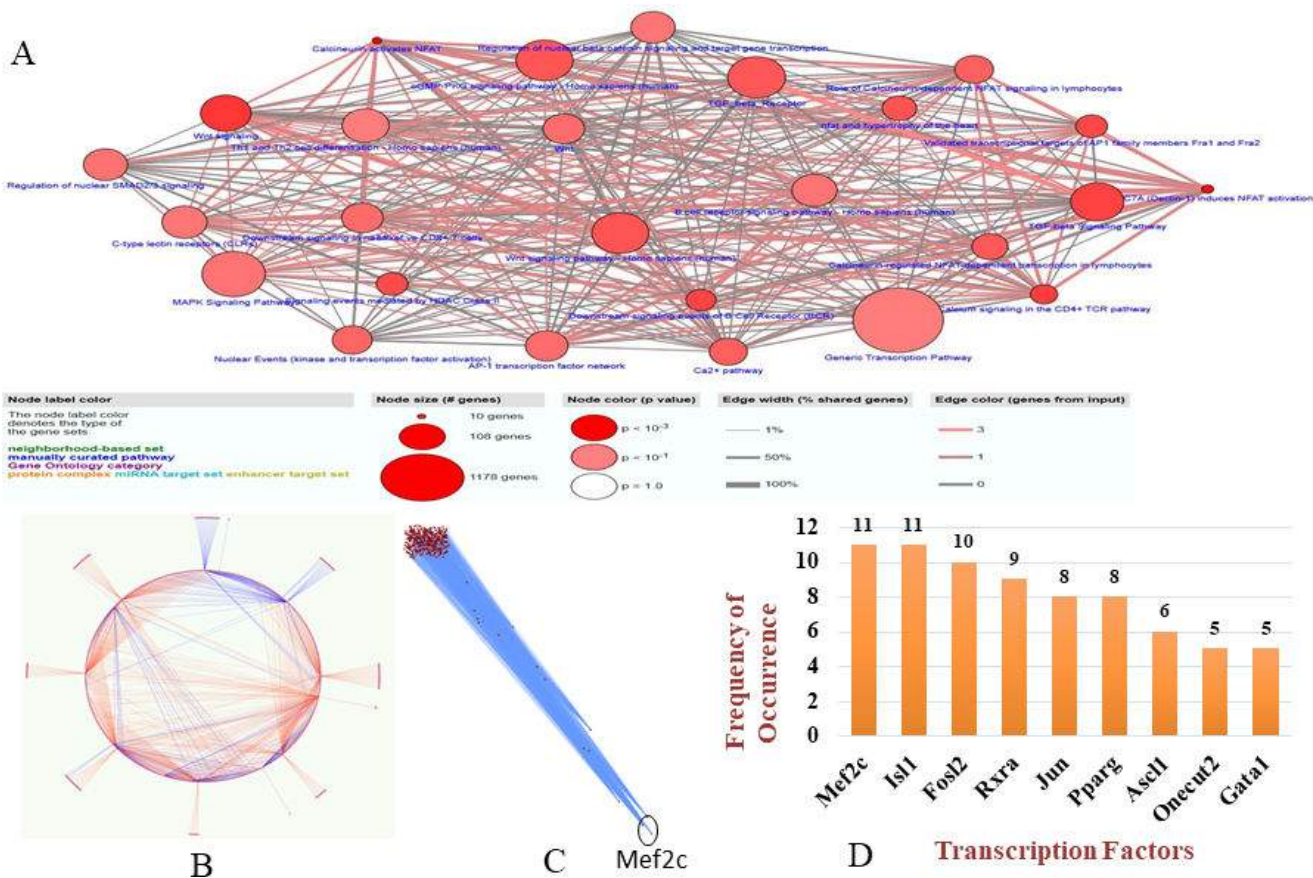
FIG 8 Transcription factor-target gene (TFTG) network analysis. (A) Pathway enrichment of sleepy macrophage genes and transcription factors (*P* value < 0.01). (B) The simulated network's circular layout demonstrating the strength of chosen transcription factors over the whole network. (C) The inter-regulatory TFTG network after running the simulated annealing algorithm, showing placement of heavily weighted nodes (TFs) positioned at the bottom of the network. (D) The top five ranked transcription factors are represented graphically, based on their frequency of occurrence according to the 12 scoring techniques of CytoHubba plugin.

DISCUSSION

The dynamics of macrophage cell clustering reveal notable shifts, depending on the time point of infection

As compared to control samples, the 6-h sample showed a similar number of clusters, although the dynamics of clusters shifted in the t-SNE plot with changes in the number of cells in individual clusters. At 12 h, cluster size and number increased with cell distribution among the 12 clusters. At 18 h, cluster number changed to 10. We do not have any apparent reason for this change; we predict that the macrophage plasticity was modulated by the parasite so that number of cells in a particular cluster increases so the number of phenotypic macrophages decreases.

Reciprocal relationship between IL-10 and IL-12 was observed during *L. major* infection

Two main phenotypes of macrophages are pro-inflammatory cytokine-expressing macrophages and anti-inflammatory cytokine-expressing macrophages, which offer inflammatory and regulatory roles, respectively, in leishmaniasis. They differ mainly in production of chemokines and cytokines, transcription factors, and specific markers, which identify their function (24). IFN-γ is expressed in pro-inflammatory cytokine-expressing macrophage phenotypes (33); CD80 is an expression marker of these
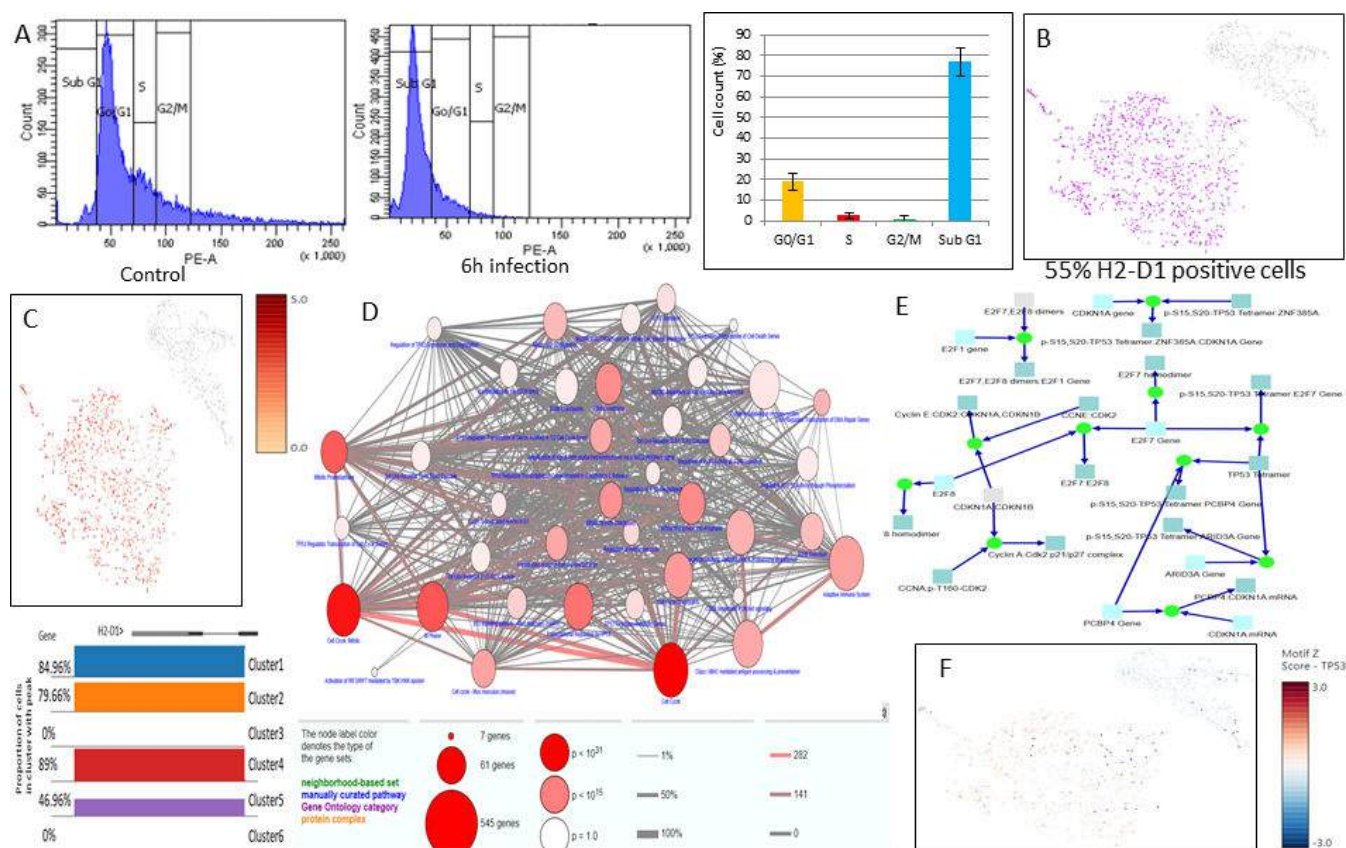
FIG 9 (A) Cell cycle analysis of RAW264.7 cells infected with *L. major* for 6 h and identification of percentage of population (results obtained are from three individual experiments). (B) t-distributed stochastic neighbor embedding (t-SNE) map of H2-D1 expression. (C) Promoter accessibility and motif *z*-score of H2-D1 population. (D) Gene ontology associated with HOXA9 (*P* value < 0.001). (E) Cell cycle analysis of sleepy macrophages shows reactions favoring G0/G1 phase. (F) TP53 motif accessibility and expression at 6 h post-infection with *L. major* (*P* value < 0.01).

macrophages (34), whereas IL-10 is commonly expressed in all anti-inflammatory cytokine-expressing macrophage subtypes (24, 35). Hence, we used them to identify overall parasite-eliminating and parasite survival-promoting macrophage subtypes at all time points and observed the dominance of anti-inflammatory cytokine-expressing macrophages over pro-inflammatory cytokine-expressing macrophage populations which might be attributed to amastigote-driven modulation of macrophage plasticity with the time of infection. Identification of both macrophage subsets was one of our novel findings as categorization of macrophage subtypes was possible through sophisticated parameters provided by scATAC-seq. Typically, log2 values harnessed are set as more than 0.5 (36), but we set threshold as 1 to ensure capturing of specific subtypes of macrophages and to avoid identification of mixed population. M2a enrichment suggested that IL-10 and arginase were overexpressed and inducted. Increased IL-10 levels and decreased IL-12 expression have been demonstrated by M2d enrichment.

IL-10 expression appears to be more prevalent in *L. major* infection

From the macrophage subtype expression paradigm, we wanted to identify the populations which were potent in expressing IL-10 and IL-12. Hence, we filtered the population which either expressed IL-10 or IL-12 to avoid overlap of populations. The sudden increase of IL-12 producing macrophages at 12 h post-infection suggested that macrophages were trying to combat infection; nonetheless, their population subsided at 18 h due to overexpression of IL-10 by the majority of the population.
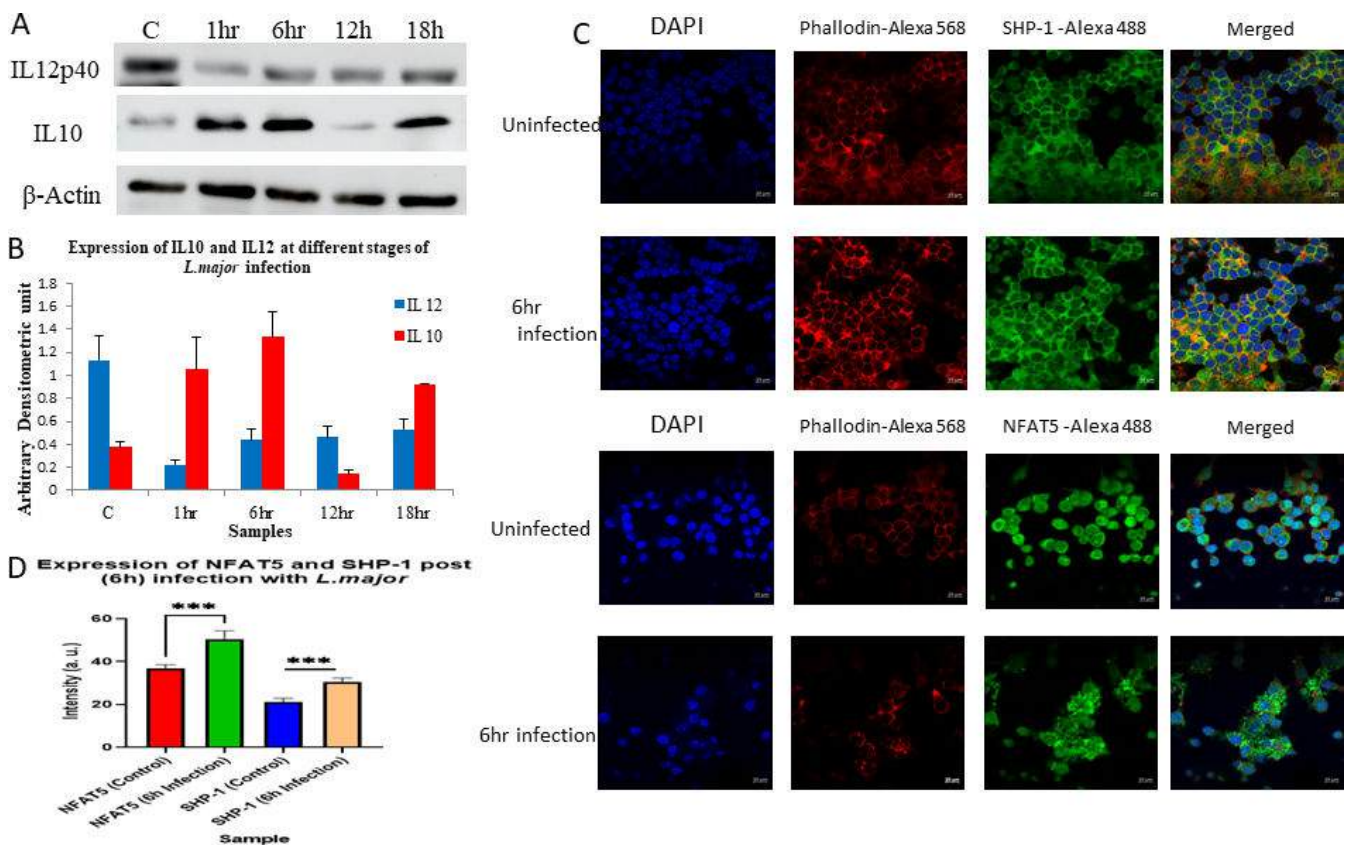
FIG 10 (A) Expression analysis of IL-10 and IL-12p40 on peritoneal macrophages infected with *L. major* at different time points. (B) Densitometry analysis of blots. (C) Localized expression of SHP-1 and NFAT5 in RAW264.7 cells. (D) Intensity measure of expression of SHP-1 and NFAT5 (P value < 0.01).

Reciprocal modulation in the expression of IL-10 and IL-12 appears evident following 6 h of infection

Using systems-based discrete mathematical models, we had previously reported about the modulation of IL-10 and IL-12 by NFAT5 and SHP-1 in *L. major* infection models. In order to facilitate the elimination of parasites, NFAT5, a transcription factor and chromatin remodeling inducer, modifies nucleosomes 1 and 2 of the IL-12b gene and the IL-10 promoter region. Later, as a mechanism to combat infection and regulate pro-inflammatory cytokine, *Leishmania* may modulate host machinery to activate SHP-1, a phosphatase, and to inactivate NFAT5, and therefore the chromatin architecture changes entirely, which activates the IL-10 gene (26). Our systems-based findings were validated when we observed expressional changes in IL-10 and IL-12 expression post-*L. major* infection from 1 h post-infection until 48 h, with major changes occurring at 6, 12, and 18 h (28).

The expression-based findings from scATAC-seq data corroborate with our data. We checked co-expression of the parasite-eliminating group, which included IL-12, NFAT5, and iNOS genes, comparatively with the parasite survival-favoring group, which included IL-10, SHP-1, and Arg1. Since nitric oxide production ultimately determines the fate of parasite survival, expression of iNOS and arginase was also taken into consideration while clustering. At 6 h, we observed parasite-eliminating macrophages dominating with further decline in the population at 12 h. Switch in macrophage population from parasite eliminating to parasite survival occurred at 18 h. Thus, this study unveiled the importance of time-dependent cellular changes which lead to leishmaniasis.

Sleepy macrophages appear to act as a cellular switch of macrophage phenotypes by regulating cell plasticity

Systematically, we started analyzing all the samples for their expression pattern. We checked the expression of housekeeping genes ActB and GAPDH; unexpectedly, we observed that Clusters 3 and 6 from the 6-h sample do not express housekeeping genes. To our surprise, these cells did not express IL-12b, IL-10, Ptpn6 (SHP-1), and Nfat5, although the motif z-score for NFAT5 was highest in these two clusters than across any other cluster in the same sample. These unique clusters were absent in other samples. Since these clusters consisted overall 28% of the population, we got intrigued about the set of genes these clusters express, transcription factors associated with these genes, pathways which are active in these clusters, and most importantly, crucial components in these clusters which are making them unique to such behavior. How the cells are managing to survive without expressing housekeeping genes is still not well understood and needs further investigation. We predict that amastigotes inside these macrophages are activating gene sets which may be conferring to their uniqueness. Even though we could identify sleepy macrophages, the mechanistic insight behind their phenotype is still not well understood. These cells did not show expression for Caspase 3 and Caspase 7, which are apoptotic markers, suggesting that sleepy macrophages were not pro-apoptotic but may be modulatory (Fig. S5).

Principal component analysis revealed cluster 3 and its genes may be critical for sleepy macrophages

Our initial finding from PCA was that the genes elevated in Clusters 3 and 6 were downregulated in Clusters 1, 2, 4, and 5. Hence, to identify which cluster is essential, we performed the PCA and observed that 85.2% of information is retained by first three clusters. From the variable plot, we can also say that Cluster 3 is negatively correlated with other clusters with high cos2 value. As an individual PC, Cluster 3 is highly correlated with PC1 and PC2, and Cluster 6 had lesser correlation, suggesting its low contribution in the data set. We distributed the PCs based on significance of their expression and categorized 814 genes in a group of five for all clusters of which genes having P values of more than 0.0001 were identified, and they showed low redundancy distribution. Hence, from this analysis, we focused our studies on Cluster 3 to identify behavior of sleepy macrophages.

Sleepy macrophages might act as transient state to prepare macrophages to combat *L. major* infection

Using GSEA we were able to analyze the defined set of genes from the 6-h sample by measuring statistically significant and concordant changes between phenotypes (sleepy macrophage and normal). GSEA was used to evaluate the relevance of numerous aberrations in gene expression and cellular transcriptional responses using single-cell ATAC gene expression data set for *Mus musculus* macrophage. Using the gene expression profiles of infected macrophages, GCT, GMT, and CLS files were prepared as input files for GSEA analysis (Tables S4 and S5). The metric used for ranking the genes in the data set was Diff_of_Classes, and the chip platform provided for the analysis was Mouse_NCBI_Gene_ID_MSigDB.v2022.1.Mm.chip. The results obtained showed that the genes belonging to Clusters 3 and 6 were positively correlated with the sleepy macrophage phenotype or state.

We analyzed the top 10 genes from the heat map by excluding pseudogenes and observed that Pcdh11x was enriched in Cluster 3, which is responsible for cell recognition and activation of PI3k/Akt signaling (37); Taf2 is critical in formation of RNA polymerase II initiation complex (38); TMEM117 primarily functions in the endoplasmic reticulum stress-mediated mitochondrial apoptotic pathway (39); Gabrg1 has a role in chloride channel activity, although we could not find its relevance in leishmaniasis or macrophages; Tox is a DNA-binding protein associated with control of the chromatin

structure, majorly in the activation of T cells (40); Fastkd3 is an unusual RNA-binding protein that critically regulates mitochondrial RNA metabolism (41); the *L. major*-infected mice model has been reported to show significant reduction in parasite burden in lymph nodes, spleen, and liver when Map2 activity was enhanced *in vivo* (42); Erap2 acts as protease to cleave antigens and form peptides which are presented by MHC-I in canine leishmaniasis (43); Zfp606 has not been reported to have any role; and Vmn2r70 is predicted to have a role in enabling G protein-coupled receptor activity. From the expression set, we could infer that sleepy macrophages may have a stressful environment; they may be undergoing epigenetic and transcriptional changes to *L. major* infection.

NFAT5 may control cellular signaling and epigenetically regulate sleepy macrophages as a response to *L. major* infection

Mef2c has been demonstrated to be associated with enrichment of classical activated macrophages that promote pro-inflammatory cytokine production in leishmaniasis (44). It was observed from patient samples that synthesis of Mef2c is associated with the NFAT5 canonical pathway, which also in turn regulates NFAT5-mediated immune response; TNF-α is the upstream regulator of MEF2C (45). In human and murine fibroblasts, Mef2c was reported to be activated at the G0/G1 phase (46). Another transcription factor which was enriched through TFTG network was Isl1, although much is not known about the role of this gene in leishmaniasis. Nonetheless, it consists of the LIM domain, which is essential for regenerating T cells in spleen in leishmaniasis (47). From the pathway enrichment analysis of all 814 genes and 51 transcription factors, we observed that NFAT5 signaling, gene transcription, MAPK signaling, and TGF-β signaling were enhanced. From this analysis, we could infer that NFAT5-mediated signaling and immune response prevail in sleepy macrophages.

TP53-mediated cell cycle irregularities in sleepy macrophages may impact immune cell activation

From cell cycle analysis of the 6-h sample, the presence of cells in sub-G1 cells identified apoptotic cells, which corroborates with Fig. S1. Cluster 3 sleepy macrophage accounts for 19%, which was also identified through the cell cycle analysis of the 6-h sample. The reactions enriched in sleepy macrophages favored the G1 phase of the cell cycle (Fig. 9E) Therefore, it may be possible that sleepy macrophages are in the G0/G1 phase (Fig. 9A). As p53 expression was pertinent in some sleepy macrophages, they may lead to G1 cell cycle arrest as it has been reported in leishmaniasis (48) at the G1 phase (49). H2-D is involved in CD8$^+$ T-cell activation and CD4$^+$ Th1 response in leishmaniasis (50, 51). H2-D1 downregulation was an intimation of decreased or irregular antigen processing and presentation and challenged the abilities of macrophages to act as antigen presenting cells when in sleepy state. These results indicated that parasites may regulate the MHC-II expression in hosts as a shielding mechanism to later grow and proliferate, and this may be strongly associated with the transcription factor and their target genes, which are associated with the cell cycle regulation and chromatin remodeling.

Expression of IL-10, IL-12, NFAT5, and SHP-1 reveals similar expression trend at protein level as identified from sc-ATAC sequencing expression analysis

From our previously reported finding (28), we observed the expression change of IL-10, IL-12, and SHP-1 with different time points of infection. Correspondingly, we observed the same trend in peritoneal macrophages with the same time points of infection. Perhaps, it may be possible that RAW264.7 cells and peritoneal macrophages may respond to infection in an identical way at the same time points. This may propose a possibility of sleepy macrophage depicting behavior in peritoneal macrophages as derivation of RAW264.7 cells was from pristane-elicited peritoneal cells of Balb/c mice (52). RAW264.7 cells also show parallel immune response to primary murine bone-

derived macrophages through TLR 2 and TLR 4 signaling (53), which is a key to CL infection from our previously reported mathematical models (26).

Conclusion

Our findings identified sleepy macrophages which possess a state adaptation to *L. major* infection. These cells boast pro-inflammatory cytokine expression by promoting chromatin remodeling and RNA regulation through transcription factors. One such transcription factor which we have highlighted from our findings is NFAT5 that dictates IL-10 and IL-12 reciprocal regulation in *L. major* infection. Often NFAT5 gets downregulated by *L. major*-induced SHP-1-mediated dephosphorylation of its auxillary export domain. It may be upright to target NFAT5 so as to direct adequate parasite elimination response. We presume that inhibition of SHP-1 may prevent NFAT5 inhibition and suppress parasite survival. Our previous work has already underlined the proposition in which peptides will be used to inhibit SHP-1. In the future, we will inspect the efficacy of peptides on macrophage populations in *L. major* infection.

AUTHOR AFFILIATION

[1]Systems Medicine Lab, National Centre for Cell Science, SP Pune University Campus, Pune, India

AUTHOR ORCIDs

Shailza Singh http://orcid.org/0000-0003-3817-8819

AUTHOR CONTRIBUTIONS

Shweta Khandibharad, Data curation, Formal analysis, Investigation, Methodology, Software, Validation, Visualization, Writing – original draft, Writing – review and editing | Shailza Singh, Conceptualization, Data curation, Formal analysis, Funding acquisition, Investigation, Methodology, Project administration, Resources, Software, Supervision, Validation, Visualization, Writing – review and editing

DATA AVAILABILITY

This Single Cell ATAC sequencing project raw files have been deposited in the National Center for Biotechnology Information Sequence Read Archive under accession number PRJNA1061857. The deposited sequence may be found in https://www.ncbi.nlm.nih.gov/bioproject/PRJNA1061857. Any data that support the findings of this study beyond what is included in the supplemental information are available from the corresponding author upon request.

ADDITIONAL FILES

The following material is available online.

Supplemental Material

Supplemental figures (Spectrum03478-23-s0001.docx). Figures S1 to S5.
Supplemental tables (Spectrum03478-23-s0002.xlsx). Tables S1 to S8.

REFERENCES

1. Andersen L, Corazon SSS, Stigsdotter UKK. 2021. Nature exposure and its effects on immune system functioning: a systematic review. Int J Environ Res Public Health 18:1416. https://doi.org/10.3390/ijerph18041416

2. Baker RE, Mahmud AS, Miller IF, Rajeev M, Rasambainarivo F, Rice BL, Takahashi S, Tatem AJ, Wagner CE, Wang L-F, Wesolowski A, Metcalf CJE. 2022. Infectious disease in an era of global change. Nat Rev Microbiol 20:193–205. https://doi.org/10.1038/s41579-021-00639-z

3. J B, M BM, Chanda K. 2021. An overview on the therapeutics of neglected infectious diseases-leishmaniasis and chagas diseases. Front Chem 9:622286. https://doi.org/10.3389/fchem.2021.622286

4. Curtin JM, Aronson NE. 2021. Leishmaniasis in the United States: emerging issues in a region of low endemicity. Microorganisms 9:578. https://doi.org/10.3390/microorganisms9030578

5. Sundar S, Singh B. 2018. Emerging therapeutic targets for treatment of leishmaniasis. Expert Opin Ther Targets 22:467–486. https://doi.org/10.1080/14728222.2018.1472241

6. Afrin F, Khan I, Hemeg HA. 2019. *Leishmania*-host interactions-an epigenetic paradigm. Front Immunol 10:492. https://doi.org/10.3389/fimmu.2019.00492

7. Masina S, M Gicheru M, Demotz SO, Fasel NJ. 2003. Protection against cutaneous leishmaniasis in outbred vervet monkeys using a recombinant histone H1 antigen. J Infect Dis 188:1250–1257. https://doi.org/10.1086/378677

8. Baharia RK, Tandon R, Sahasrabuddhe AA, Sundar S, Dube A. 2021. Correction: nucleosomal histone proteins of *L. donovani*: a combination of recombinant H2A, H2B, H3 and H4 proteins were highly immunogenic and offered optimum prophylactic efficacy against *Leishmania* challenge in hamsters. PLoS One 16:e0252177. https://doi.org/10.1371/journal.pone.0252177

9. Almeida L, Silva JA, Andrade VM, Machado P, Jamieson SE, Carvalho EM, Blackwell JM, Castellucci LC. 2017. Analysis of expression of FLI1 and MMP1 in American cutaneous leishmaniasis caused by *Leishmania braziliensis* infection. Infect Genet Evol 49:212–220. https://doi.org/10.1016/j.meegid.2017.01.018

10. Mukherjee S, Mukherjee B, Mukhopadhyay R, Naskar K, Sundar S, Dujardin J-C, Roy S. 2014. Imipramine exploits histone deacetylase 11 to increase the IL-12/IL-10 ratio in macrophages infected with antimony-resistant *Leishmania donovani* and clears organ parasites in experimental infection. J Immunol 193:4083–4094. https://doi.org/10.4049/jimmunol.1400710

11. Chen H, Lareau C, Andreani T, Vinyard ME, Garcia SP, Clement K, Andrade-Navarro MA, Buenrostro JD, Pinello L. 2019. Assessment of computational methods for the analysis of single-cell ATAC-seq data. Genome Biol 20:241. https://doi.org/10.1186/s13059-019-1854-5

12. Fang R, Preissl S, Li Y, Hou X, Lucero J, Wang X, Motamedi A, Shiau AK, Zhou X, Xie F, Mukamel EA, Zhang K, Zhang Y, Behrens MM, Ecker JR, Ren B. 2021. Comprehensive analysis of single cell ATAC-seq data with SnapATAC. Nat Commun 12:1337. https://doi.org/10.1038/s41467-021-21583-9

13. Rai V, Quang DX, Erdos MR, Cusanovich DA, Daza RM, Narisu N, Zou LS, Didion JP, Guan Y, Shendure J, Parker SCJ, Collins FS. 2020. Single-cell ATAC-seq in human pancreatic islets and deep learning upscaling of rare cells reveals cell-specific type 2 diabetes regulatory signatures. Mol Metab 32:109–121. https://doi.org/10.1016/j.molmet.2019.12.006

14. Wu X, Lu M, Yun D, Gao S, Chen S, Hu L, Wu Y, Wang X, Duan E, Cheng CY, Sun F. 2022. Single-cell ATAC-seq reveals cell type-specific transcriptional regulation and unique chromatin accessibility in human spermatogenesis. Hum Mol Genet 31:321–333. https://doi.org/10.1093/hmg/ddab006

15. Mulqueen RM, Pokholok D, O'Connell BL, Thornton CA, Zhang F, O'Roak BJ, Link J, Yardımcı GG, Sears RC, Steemers FJ, Adey AC. 2021. High-content single-cell combinatorial indexing. Nat Biotechnol 39:1574–1580. https://doi.org/10.1038/s41587-021-00962-z

16. Jia G, Preussner J, Chen X, Guenther S, Yuan X, Yekelchyk M, Kuenne C, Looso M, Zhou Y, Teichmann S, Braun T. 2018. Single cell RNA-seq and ATAC-seq analysis of cardiac progenitor cell transition states and lineage settlement. Nat Commun 9:4877. https://doi.org/10.1038/s41467-018-07307-6

17. Pott S, Lieb JD. 2015. Single-cell ATAC-seq: strength in numbers. Genome Biol 16:172. https://doi.org/10.1186/s13059-015-0737-7

18. Xu W, Wen Y, Liang Y, Xu Q, Wang X, Jin W, Chen X. 2021. A plate-based single-cell ATAC-seq workflow for fast and robust profiling of chromatin accessibility. Nat Protoc 16:4084–4107. https://doi.org/10.1038/s41596-021-00583-5

19. Zhu T, Liao K, Zhou R, Xia C, Xie W. 2020. ATAC-seq with unique molecular identifiers improves quantification and footprinting. Commun Biol 3:675. https://doi.org/10.1038/s42003-020-01403-4

20. Baek S, Lee I. 2020. Single-cell ATAC sequencing analysis: from data preprocessing to hypothesis generation. Comput Struct Biotechnol J 18:1429–1439. https://doi.org/10.1016/j.csbj.2020.06.012

21. Baker SM, Rogerson C, Hayes A, Sharrocks AD, Rattray M. 2019. Classifying cells with Scasat, a single-cell ATAC-seq analysis tool. Nucleic Acids Res 47:e10. https://doi.org/10.1093/nar/gky950

22. Liu D, Uzonna JE. 2012. The early interaction of *Leishmania* with macrophages and dendritic cells and its influence on the host immune response. Front Cell Infect Microbiol 2:83. https://doi.org/10.3389/fcimb.2012.00083

23. Khandibharad S, Nimsarkar P, Singh S. 2022. Mechanobiology of immune cells: messengers, receivers and followers in leishmaniasis aiding synthetic devices. Curr Res Immunol 3:186–198. https://doi.org/10.1016/j.crimmu.2022.08.007

24. Tomiotto-Pellissier F, Bortoleti B da S, Assolini JP, Gonçalves MD, Carloto ACM, Miranda-Sapla MM, Conchon-Costa I, Bordignon J, Pavanelli WR. 2018. Macrophage polarization in leishmaniasis: broadening horizons. Front Immunol 9:2529. https://doi.org/10.3389/fimmu.2018.02529

25. Loría-Cervera EN, Andrade-Narvaez F. 2020. The role of monocytes/macrophages in *Leishmania* infection: a glance at the human response. Acta Trop 207:105456. https://doi.org/10.1016/j.actatropica.2020.105456

26. Khandibharad S, Singh S. 2021. Computational system level approaches for discerning reciprocal regulation of IL10 and IL12 in leishmaniasis. Front Genet 12:784664. https://doi.org/10.3389/fgene.2021.784664

27. Kamhawi S, Serafim TD. 2020. *Leishmania*: a maestro in epigenetic manipulation of macrophage inflammasomes. Trends Parasitol 36:498–501. https://doi.org/10.1016/j.pt.2020.04.008

28. Khandibharad S, Singh S. 2022. Artificial intelligence channelizing protein-peptide interactions pipeline for host-parasite paradigm in IL-10 and IL-12 reciprocity by SHP-1. Biochim Biophys Acta Mol Basis Dis 1868:166466. https://doi.org/10.1016/j.bbadis.2022.166466

29. Lê S, Josse J, Husson F. 2008. FactoMineR: an R package for multivariate analysis. J Stat Softw 25:1–18. https://doi.org/10.18637/jss.v025.i01

30. Subramanian A, Tamayo P, Mootha VK, Mukherjee S, Ebert BL, Gillette MA, Paulovich A, Pomeroy SL, Golub TR, Lander ES, Mesirov JP. 2005. Gene set enrichment analysis: a knowledge-based approach for interpreting genome-wide expression profiles. Proc Natl Acad Sci U S A 102:15545–15550. https://doi.org/10.1073/pnas.0506580102

31. Zito A, Lualdi M, Granata P, Cocciadiferro D, Novelli A, Alberio T, Casalone R, Fasano M. 2021. Gene set enrichment analysis of interaction

networks weighted by node centrality. Front Genet 12:577623. https://doi.org/10.3389/fgene.2021.577623

32. Fukushima A. 2013. DiffCorr: an R package to analyze and visualize differential correlations in biological networks. Gene 518:209–214. https://doi.org/10.1016/j.gene.2012.11.028

33. Orecchioni M, Ghosheh Y, Pramod AB, Ley K. 2019. Macrophage polarization: different gene signatures in M1(LPS+) vs. classically and M2(LPS-) vs. alternatively activated macrophages. Front Immunol 10:1084. https://doi.org/10.3389/fimmu.2019.01084

34. Atri C, Guerfali FZ, Laouini D. 2018. Role of human macrophage polarization in inflammation during infectious diseases. Int J Mol Sci 19:1801. https://doi.org/10.3390/ijms19061801

35. Lopes RL, Borges TJ, Zanin RF, Bonorino C. 2016. IL-10 is required for polarization of macrophages to M2-like phenotype by mycobacterial DnaK (heat shock protein 70). Cytokine 85:123–129. https://doi.org/10.1016/j.cyto.2016.06.018

36. Merrill CB, Montgomery AB, Pabon MA, Shabalin AA, Rodan AR, Rothenfluh A. 2022. Harnessing changes in open chromatin determined by ATAC-seq to generate insulin-responsive reporter constructs. BMC Genomics 23:399. https://doi.org/10.1186/s12864-022-08637-y

37. Wei X, Yuan Y, Yang Q. 2022. SNHG22 promotes migration and invasion of trophoblasts via miR-128-3p/PCDH11X axis and activates PI3K/Akt signaling pathway. Clinics (Sao Paulo) 77:100055. https://doi.org/10.1016/j.clinsp.2022.100055

38. Alpern D, Langer D, Ballester B, Le Gras S, Romier C, Mengus G, Davidson I. 2014. TAF4, a subunit of transcription factor II D, directs promoter occupancy of nuclear receptor HNF4A during post-natal hepatocyte differentiation. Elife 3:e03613. https://doi.org/10.7554/eLife.03613

39. Maruyama R, Kiyohara Y, Kudo Y, Sugiyama T. 2023. Effects of the anti-inflammatory drug celecoxib on cell death signaling in human colon cancer. Naunyn Schmiedebergs Arch Pharmacol 396:1171–1185. https://doi.org/10.1007/s00210-023-02399-4

40. Yu X, Li Z. 2015. TOX gene: a novel target for human cancer gene therapy. Am J Cancer Res 5:3516–3524.

41. Boehm E, Zornoza M, Jourdain AA, Delmiro Magdalena A, García-Consuegra I, Torres Merino R, Orduña A, Martín MA, Martinou J-C, De la Fuente MA, Simarro M. 2016. Role of FAST kinase domains 3 (FASTKD3) in post-transcriptional regulation of mitochondrial gene expression. J Biol Chem 291:25877–25887. https://doi.org/10.1074/jbc.M116.730291

42. Le Pape P. 2008. Development of new antileishmanial drugs--current knowledge and future prospects. J Enzyme Inhib Med Chem 23:708–718. https://doi.org/10.1080/14756360802208137

43. Pedersen NC, Dhanota JK, Liu H. 2016. Polymorphisms in ERAP1 and ERAP2 are shared by Caninae and segregate within and between random- and pure-breeds of dogs. Vet Immunol Immunopathol 179:46–57. https://doi.org/10.1016/j.vetimm.2016.08.006

44. Dirkx L, Hendrickx S, Merlot M, Bulté D, Starick M, Elst J, Bafica A, Ebo DG, Maes L, Van Weyenbergh J, Caljon G. 2022. Long-term hematopoietic stem cells as a parasite niche during treatment failure in visceral leishmaniasis. Commun Biol 5:626. https://doi.org/10.1038/s42003-022-03591-7

45. Salih MAM, Fakiola M, Lyons PA, Younis BM, Musa AM, Elhassan AM, Anderson D, Syn G, Ibrahim ME, Blackwell JM, Mohamed HS. 2017. Expression profiling of Sudanese visceral leishmaniasis patients pre- and post-treatment with sodium stibogluconate. Parasite Immunology 39. https://doi.org/10.1111/pim.12431

46. Di Giorgio E, Gagliostro E, Clocchiatti A, Brancolini C. 2015. The control operated by the cell cycle machinery on MEF2 stability contributes to the downregulation of CDKN1A and entry into S phase. Mol Cell Biol 35:1633–1647. https://doi.org/10.1128/MCB.01461-14

47. Golub R, Tan J, Watanabe T, Brendolan A. 2018. Origin and immunological functions of spleen stromal cells. Trends Immunol 39:503–514. https://doi.org/10.1016/j.it.2018.02.007

48. Ghosh A, Labrecque S, Matlashewski G. 2001. Protection against *Leishmania donovani* infection by DNA vaccination: increased DNA vaccination efficiency through inhibiting the cellular p53 response. Vaccine 19:3169–3178. https://doi.org/10.1016/s0264-410x(01)00023-8

49. Kuzmenok OI, Chiang S-C, Lin Y-C, Lee ST. 2005. Retardation of cell cycle progression of macrophages from G1 to S phase by ICAM-L from *Leishmania*. Int J Parasitol 35:1547–1555. https://doi.org/10.1016/j.ijpara.2005.08.006

50. Nico D, Gomes DC, Palatnik-de-Sousa I, Morrot A, Palatnik M, Palatnik-de-Sousa CB. 2014. *Leishmania donovani* nucleoside hydrolase terminal domains in cross-protective immunotherapy against *Leishmania amazonensis* murine infection. Front Immunol 5:273. https://doi.org/10.3389/fimmu.2014.00273

51. Zhang J, He J, Li J, Zhou Q, Chen H, Zheng Z, Chen Q, Chen D, Chen J, Ho PL. 2020. The immunogenicity and protective immunity of multi-epitopes DNA prime-protein boost vaccines encoding Amastin-Kmp-11, Kmp11-Gp63 and Amastin-Gp63 against visceral leishmaniasis. PLoS One 15:e0230381. https://doi.org/10.1371/journal.pone.0230381

52. Rouzer CA, Ivanova PT, Byrne MO, Milne SB, Marnett LJ, Brown HA. 2006. Lipid profiling reveals arachidonate deficiency in RAW264.7 cells: structural and functional implications. Biochemistry 45:14795–14808. https://doi.org/10.1021/bi061723j

53. Berghaus LJ, Moore JN, Hurley DJ, Vandenplas ML, Fortes BP, Wolfert MA, Boons G-J. 2010. Innate immune responses of primary murine macrophage-lineage cells and RAW 264.7 cells to ligands of toll-like receptors 2, 3, and 4. Comp Immunol Microbiol Infect Dis 33:443–454. https://doi.org/10.1016/j.cimid.2009.07.001

Mechanistic study of inhibitory peptides with SHP-1 in hypertonic environment for infection model

Shweta Khandibharad, Shailza Singh [*]

Systems Medicine Laboratory, Biotechnology Research and Innovation Council- National Centre for Cell Science, NCCS Complex, Ganeshkhind, SPPU Campus, Pune 411007, INDIA

ARTICLE INFO

ABSTRACT

Cutaneous Leishmaniasis, an infectious disease is globally the most prevalent form of leishmaniasis accounting for approximately 1 million cases every year as per world health organization. Infected individuals develop skin lesion which has been reported to be infiltrated by immune cells and parasite with high sodium accumulation creating hypertonic environment. In our work, we tried to mimic the hypertonic environment in virtual environment to study dynamicity of SHP-1 and NFAT5 along with their interactions through molecular dynamics simulation. We validated the SHP-1 and NFAT5 dynamics in infection and HSD conditions to study the impact of hypertonicity derived NFAT5 mediated response to *L.major* infection. We also evaluated our therapeutic peptides for their binding to SHP-1 and to form stable complex. Membrane stability with the peptides was analyzed to understand their ability to sustain mammalian membrane. We identified PepA to be a potential candidate to interact with SHP-1. Inhibition of SHP-1 through PepA to discern IL-10 and IL-12 reciprocity may be assessed in future and furnish us with a potential therapeutic molecule. HSD mice exhibited high pro-inflammatory response to *L.major* infection which resulted in reduced lesion size. Contrary to observations in HSD mice, infection model exhibited low pro-inflammatory response and increased lesion size with high parasite load. Thus, increase in NFAT5 expression and reduced SHP-1 expression may result in disease resolving effect which can be further studied through incorporation of synthetic circuit using PepA to modulate IL-10 and IL-12 reciprocity.

1. Introduction

The development of therapeutically effective drugs has benefited tremendously by computer-aided drug discovery and design techniques [1]. The drug target's structure offers crucial information about the ligand's geometric fit into the binding site, low-energy conformation, ideal molecular electrostatic potentials, the presence of charged and/or neutral hydrogen bonds between functional groups, and hydrophobic interactions between surfaces that are lipophilic. Computational analysis becomes more difficult in both space and time when the full spectrum of molecular flexibility is taken into account hence docking algorithm which should be correctly taken into account may be more centric towards the impact of water molecules and other solvent systems [2]. The most widely used technique for protein-ligand interactions

---

include MDS, genetic algorithms, MCMC, and systematic enumeration of conformations [1].

In eukaryotic systems, a molecule can be transported through a lipid membrane by active or passive transport mechanisms although studies show that abundant number of molecules due to their kinetics are unable to cross the apical membrane [3]. To get an approximation and correlation of molecules crossing the membrane, MDS can be employed as it connects timescales and space between simulations derived three dimensional (3D)-structure data and experimentally derived one dimensional structure [4]. The algorithm suffices the environmental condition needs with an availability of varied membrane types, cellular environment confinement boundaries and molecular enrichment by salts.

Early reports of cutaneous leishmaniasis (CL) suggested that hypertonic NaCl solution was used to treat 158 acute CL lesions in 70 patients with effectiveness of 96.05% cure rate which was as efficient as sodium stibogluconate (96.42% cure rate) hence it was a strongly recommended as a low-cost, discrete, and efficient local intralesional therapeutic technique for treating CL [5]. Evidences suggested that in leishmaniasis, HSD induced sodium accumulation in skin and upregulates protective immunity through classically activated macrophages ameliorating protection against leishmaniasis [6]. Moreover, defenses against protozoan parasite *L.major* was strengthened by high salt induced NFAT5 dependent NO generation manifesting leishmanicidal activity [7]. Implications of high salt towards elimination of acute *L.major* infections *in vivo* was exhibited by NFAT5 mediated high iNOS expression substantiated by chromatin modeling of NOS2 and IL-12 [8].

Our previous findings report, NFAT5 may regulate IL-10 and IL-12 reciprocity through chromatin remodeling which can be regulated by SHP-1 [9]. Further, we could also channelize a pipeline for computational aided drug discovery and developed peptides which can inhibit SHP-1 [10]. From this article, we aim to study the efficacy of these peptides in a complex environment of hypertonicity and if they can cross the cell membrane in hypertonic environment with minimal effects on its stability by employing computational modeling and simulations. We also orient towards the propensities of our protein targets NFAT5 and SHP-1 in a physically confined environment essentially by dwelling into membrane assembled stability of NFAT5-SHP-1 interacting complex. Moreover, we checked the steadiness of NFAT5 and SHP-1 in concentration dependent osmotic pressure induced fluctuations we want to contemplate sustainability of the structure. Lastly, we wanted to evaluate our therapeutic synthetic peptides, Peptide A (PepA), Peptide B (PepB) and Peptide B (PepC) derived from artificial intelligence and machine learning approach [10] as an inhibitor for developing steady interactions with SHP-1 and cross mammalian cell membrane in hypertonic environment. Using the time-scale and space dependent barrier closing approach of MDS we aim to answer the kinetic behavior of proteins and peptides, the dynamicity of designed inhibitory peptides to cross cell membrane in hypertonic stress often observed in leishmaniasis. We developed HSD mice models and studied the effect of HSD on parasite load, cytokine expression, NO induction and macrophage population in lesion.

2. Methodology

Based on Newton's second law of motion, which states that the mass and acceleration of the atoms determine how much force is exerted, MDS creates a force field to observe behavioral changes in protein residues [11].

2.1. Protein preparation

This step prepares the protein structure and PLDS for analysis. It occurs in three crucial steps that include structure importing and processing, reviewing the protein structure followed by modifying them and lastly the structure is refined for later building a system and environment for simulation.

For processing the protein structures and PLDS the first order of action is to redefine bond order to increase accuracy of MDS by reducing inherent noise in the energy distribution of atoms [12], As experimentally discovered protein structures lack annotated hydrogen sites, they have a low electron density. As a result, hydrogens are added [13]. Addition of disulfide bond is impactful to a protein in an attempt to stabilize it is one of the most popular methods. Reduced unfolded state entropy, enthalpy improvements to the unfolded state, and kinetic stabilization of the folded state have all been linked to increases in protein stability brought on by the introduction of a disulfide bond [14]. To cap the N-termini and C-termini of the protein, non-charged groups are added to each terminal for MDS and at last any water crystals in the protein structures are removed which may show up as HETRO atom groups or "Het groups".

The protein or PLDS is followed with a review and modify step where the overall changes made in the preprocessing step was reviewed for protein and for PLDS. Moreover, the structures were refined by hydrogen bond assessment by using simplified rules of neutral pH followed by optimization through Monte Carlo search as it identifies ASN, GLN, and HIS residues are sampled in various protonation states and the OH bonds are rotated to optimize the hydrogen bond geometry. This step was significant to improve hydrogen atoms in the structure inserted from previous step by using simple geometric templates.

2.2. Construction of system for simulation through system builder

In particular MD simulation holds critical application to determine the effect of perturbations on biomolecule. Our aim was to check the effect of high salt stress on SHP-1 and NFAT5 to see if they are able to sustain inflammatory conditions, we also wanted to check if atomic motions of SHP-1 and NFAT5 interactions are stable in hyperosmolar conditions more importantly because SHP-1 inhibits translocation of NFAT5 in to the nucleus. We constructed the system not only to study the mechanistic atomic sustainability of these proteins but also to see the effect of system on atomic forcefield for our peptide based therapeutic. We wanted to address major concerns when it comes to precision therapy such as will the therapeutic peptides pose atomic and stearic properties to cross the cell membrane and nuclear membrane? Will the peptide be able to sustain hyperosmolar environment? Will the peptide bind to SHP-1 in hyperosmolar environment and form stable complex? Will the peptide show better stability and strong interactions than the already available SHP-1 inhibitor?

The solvent model used was TIP3P with buffer distance of 10 Å that is equivalent to the standard real space Coulombic interaction cutoff for computations involving long-range electrostatic fields, the membrane used was DMPC as it possesses low cholesterol molecules which is observed in nuclear membrane [15]. The Boundary shape was Orthorhombic and the entire systems volume was minimized to align along the vector axes of the simulation box. To mimic the hypertonic conditions we added 100 mM (200mOsmol/kg), 150 mM (300mOsmol/kg), 200 mM (400mOsmol/kg) and 250 mM (500mOsmol/kg) NaCl to the system.

2.3. Minimization and Molecular dynamics simulation

To achieve minimum energy configurations of molecules, we performed minimization for all the structures for 100 ns and further evaluation for structures was done using MDS. The simulations were performed on DESMOND 3.2 with maestro-v11.6 (D.E. Shaw Research) platform [16].

The structures were simulated for respective time (mentioned in results), and the ensemble class for the simulation was NPT. The temperature was set to 300 K and pressure to 1 bar. To produce high quality molecular system was set to Relax model system before simulation and MDS was done. Post simulation, RMSD, RMSF and RoG was analyzed

along with interaction paradigm.

2.4. In vitro maintenance of L.major promastigotes

L. major promastigotes (MHOM/Su73/5ASKH) were cultured in RPMI medium enriched with 20% FBS and maintained at a temperature of 27 °C. The stationary phase of promastigotes was employed for experiments related to infection.

2.5. Experimental animals

All animal studies presented in this work received approval from the animal ethics committee of the National Centre for Cell Science (NCCS), India. All animal experiments adhered to national regulations governing animal experimentation. Twenty four female Balb/c mice, aged 4–6 weeks, were utilized for the experiments and housed in the experimental animal facility at NCCS, India. The study comprised three groups including Control (Uninfected) mice ($n = 8$), *L.major* infected mice ($n = 8$), and mice which were infected with *L.major* and were supplemented with High Salt Diet (HSD) mice ($n = 8$). The Infection group was infected with 10^3 *L.major* stationary phase promastigotes in the ear pinna and monitored for 45 days prior to experimentation. HSD mice were induced by administering 1% NaCl in their drinking water throughout the experiment. Initially, for 14 days, mice were provided with 1% NaCl in drinking water, followed by infection with 10^3 *L. major* stationary phase promastigotes in the ear pinna, and observation for 30 days.

2.6. Confocal analysis

Peritoneal macrophages from all experimental animal groups were isolated and seeded on eight well chamber slides. The cells were initially rinsed using $1\times$ PBST and then treated with 4% paraformaldehyde for 20 min at room temperature to fix them. Following three washes with $1\times$ PBST, the cells were permeabilized for 10 min with PBST and subsequently blocked with 3% BSA for 30 min. Primary antibodies for SHP-1 (3759S, Cell Signaling Technology) and NFAT5 (PA1–023, Thermo Fisher Scientific) were added to the cells in a 1:1000 dilution and incubated at room temperature for 2 h. Following the incubation, the cells were washed three times with PBST and then incubated with anti-rabbit IgG (H + L) F(ab')2 fragment AlexaFluor 488 Conjugate (4412S, Cell Signaling Technology) at a 1:500 dilution and Mouse Phalloidin AlexaFluor 568 (A12380, ThermoFisher Scientific) at a 1:500 dilution for 1 h. Following incubation, the cells were washed three times with $1\times$ PBST and then counterstained with DAPI for 10 min. Subsequently, the cells were washed three times with $1\times$ PBST and three times with distilled water. Finally cells were air-dried and mounting media (00–4958-02, ThermoFisher Scientific) was added to the slides, and the cells were observed at $60\times$ and $100\times$ magnification using a Zeiss LSM 880 with Airyscan microscope. Image analysis was performed using Fiji.

2.7. Western blot

Peritoneal macrophages were isolated from Control, Infected and HSD mice followed by protein extraction using RIPA buffer. Total protein was quantified using BCA protein estimation method. Subsequently, 8% and 12% polyacrylamide gels were prepared, and a total of 20 μg of protein from all samples was loaded onto the gels and subsequently transferred to nitrocellulose membranes. The membranes were then blocked with 3% BSA for one hour. After three washes with TBST, the blots were incubated overnight at 4 °C with primary antibodies against NFAT5 (PA1–023, Thermo Fisher Scientific) and β-Actin (4967S, Cell Signaling Technology). Following three washes with TBST, the blots were further incubated with the secondary antibody, Anti-Rabbit IgG (whole molecule)–Peroxidase antibody produced in goat (A9169, Sigma-Aldrich), for one hour at room temperature. Subsequently, the blots were washed thrice with TBST and developed using Luminol-

Enhancer Solution (XLS070L, Cyanagen) and H_2O_2 (XLS070L, Cyanagen XLS070P), and images were captured using the Amersham Image-Quant 800.

2.8. Histopathological study

Cutaneous lesions were isolated from infected and HSD experimental groups and fixed with 10% formaldehyde. The lesions were treated with 70% ethanol, 95% ethanol and absolute ethanol for an hour each followed by incubation in xylene for 2 h. Later, the lesions were embedded in paraffin and sectioned into 5 μm slices. Sections were rehydrated in absolute ethanol, 95% ethanol and distilled water each for an hour. Lastly, sections were stained with H&E stains and were observed under CILIKA microscope.

2.9. Immuno-histochemistry (IHC)

Following a methodology analogous to the histopathology study, tissue sections were prepared and rehydrated. Antigen retrieval was performed by adding a solution of 0.1% trypsin in PBS to the sections, followed by 15-min incubation. After washing the sections thrice with PBS, a 3% H_2O_2 solution was added to sections and they were incubated for 15 min. After washing thrice with PBS, sections were blocked with 5% BSA for 10 min. Subsequently, the sections were incubated with NFAT5 primary antibody and SHP-1 primary antibody (3759S, Cell Signaling Technology) for an hour in a humidified chamber. After washing the sections thrice with PBS, the secondary antibody, Anti-Rabbit IgG (whole molecule)–Peroxidase antibody, was added for an hour in a humidified chamber, followed by PBS washes. 3,3′-Diaminobenzidine solution was added to the slides, and the sections were incubated for 10 min to develop colour. The sections were counterstained with hematoxylin, washed, mounted, and then observed under a CILIKA microscope.

2.10. Nitrate estimation

Sera from each experimental group were isolated to quantify the amount of NO using Griess reagent kit. In a microplate, 20 μL Griess reagent, 150 μL of sample and 130 μL of deionized water was added and incubated for 30 min at room temperature. Absorbance of samples was taken at 548 nm and nitrite concentrations were estimated.

2.11. Fluorescence activated cell sorting (FACS)

Animals were euthanized and whole external ear was isolated and kept at on ice in tubes containing $1\times$ PBS. Freshly isolated ears were washed with 70% ethanol for 5 min and further washed with $1\times$ PBS thrice. Using forceps, the inner and outer cuticular sections of the ear pinna were separated to isolate lesion in a polystyrene petri dish. Isolated lesions were homogenized in chilled $1\times$ PBS from both infected and HSD groups. Isolated cell suspension was passed through 40 μm cell strainer, to obtain single-cell suspension of the cell population residing in the lesion. The cells were washed three times with PBS containing 0.1% FBS by centrifuging cells at 2500 rpm for 10 min. Subsequently, they were incubated for one hour with a 1:100 dilution of CD163-PE antibody (12–1631-82, Thermo Fisher Scientific) and a 1:100 dilution of CD80-APC antibody (17–0801-82, Thermo Fisher Scientific). Further, cells underwent three additional washes with PBS containing 0.1% FBS before being acquired on a BD FACS Canto II instrument.

2.12. Enzyme linked immunosorbent assay (ELISA)

Sera samples from all experimental groups were analyzed to determine the levels of IL-12 and IL-10 using (IL-12 Mouse ELISA Kit BMS616, Thermo Fisher Scientific) and (IL-10 Mouse ELISA Kit BMS614, Thermo Fisher Scientific) by following the manufacturer's protocol. Briefly, sera

was diluted in a 1:1 ratio with sample diluent and combined with a 1:100 diluted Biotin-conjugated primary antibody. The mixture was then incubated on a shaker at room temperature for 2 h on coated plates. Following incubation, the wells were washed with a wash buffer, and a 1:100 dilution of Streptavidin-HRP secondary antibody was added, incubating for an additional hour, followed by washes with the wash buffer. TMB substrate was added to the wells and incubated for 10 min in dark after which stop solution was added. The colorimetric readings were obtained using a 96-well plate spectrophotometer at 450 nm.

2.13. Statistical analysis

The quantitative data represented are from representative experiments with four animal pools that were conducted at least twice having similar results. Represented data shows mean and ± standard deviation (SD) of two independent experiments at least. The Student's *t*-test for two independent samples, One-way ANOVA for 3 independent groups and two-way ANOVA for data set with two independent variables among groups were used to analyze the dataset respectively. *p*-value <0.05 indicated statistical significance for differences and were marked by asterisk. GraphPad Prism 5 for Windows, a program created by La Jolla, California-based GraphPad Software (www.graphpad.com), was used for all data analysis.

3. Results

To understand if NFAT5 and SHP-1 structures are stable in increasing osmolality in cytoplasmic environment, we performed MDS for NFAT5 structure which consisted of AED and DBD as both the structures crucially promotes translocation of this transcription factor from cytoplasm to nucleus and binds to promoter region of genes. C-terminal truncated structure of SHP-1 consisting 594 amino acids was simulated as parasite GP63 cleaves it at serine 594 position [17] [18] therefore

high prevalence of truncated SHP-1 in cytoplasm may occur which was taken into consideration for simulation.

In Fig. 1, an increase in RMSD and minor fluctuations in truncated SHP-1 structure was observed in hypertonic conditions although the structure retained its conformations throughout the simulation (Fig. 1A). RMSF at N-terminal amino acid was higher as compared to other amino acids (Fig. 1B). RoG in hypertonic condition had lower fluctuations post 500 ns trajectory suggesting, SHP-1 structure was more compact in hypertonic condition (Fig. 1C). NFAT5 gets activated in hypertonic environment and release pro-inflammatory cytokines [19] and RMSD of NFAT5 in increasing osmotic stress shows increase in stability and reduction of fluctuation in the structure (Fig. 1D). RMSF shows high fluctuation at 250 position of amino acid and RoG also decreased with increase in osmolality indicating, NFAT5 structure was compact during simulation and amino acid fluctuation from their mean structure was lower (Fig. 1E and F). The structure of NFAT5 was also stable without changing the secondary structure (Fig. 1G-1J). Representative image of NFAT5 in normal condition as compared to hypertonic condition is represented in (Fig. 1G and H) which shows the structural stability of NFAT5 is more compact in hypertonic environment. Similarly, quaternary structure of SHP-1 was observed to be stable in hypertonic environment (Fig. 1I and J). Therefore, we further studied the interaction of both proteins in hypertonic conditions.

SHP-1 may inhibit NFAT5 by dephosphorylating it at tyrosine 143 residue [20] and inhibit the translocation to nucleus which may inactivate pro-inflammatory cytokine secretion and may lead to IL-10 secretion [9] [10]. Our previous work has identified that phosphatase domain of SHP-1 may interact with auxiliary export domain of NFAT5 [10]. Hence we simulated the docked complex of AED_DBD_NFAT5 with truncated SHP-1 for 200 ns in normal osmotic conditions and in hypertonic condition with insertion of DMPC membrane. RMSD of complex was stable throughout the trajectory in hypertonic condition (Fig. 2A). RMSF and RoG of complex were also stable (Fig. 2B and C).
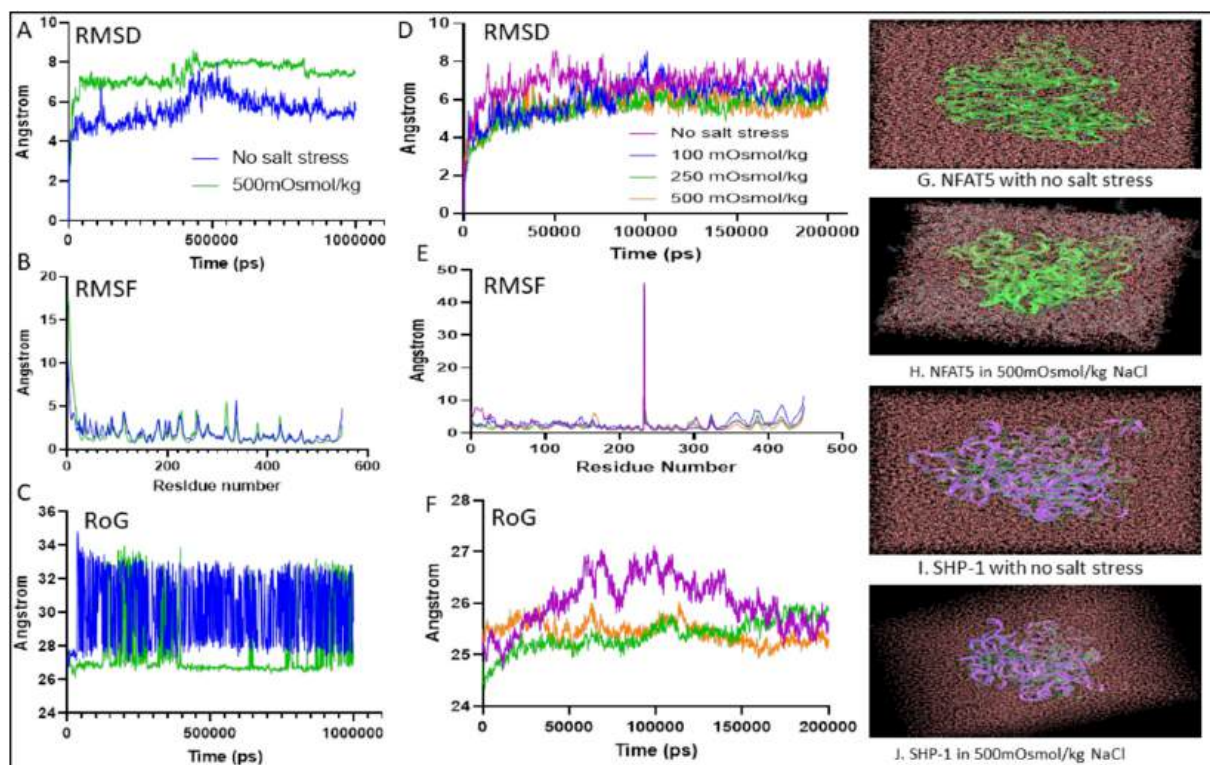

Fig. 1. (A-C) RMSD, RMSF and RoG of truncated SHP-1 with and without hyperosmotic stress. (D—F) RMSD, RMSF and RoG of AED_DBD_NFAT5 with increasing osmolality (G and I) AED_DBD_NFAT5 and truncated SHP-1 structure post 200 ns and 1 μs simulation. (H and J) AED_DBD_NFAT5 and truncated SHP-1 structure at 500mOsmol/kg NaCl environment post 200 ns and 1 μs simulation.
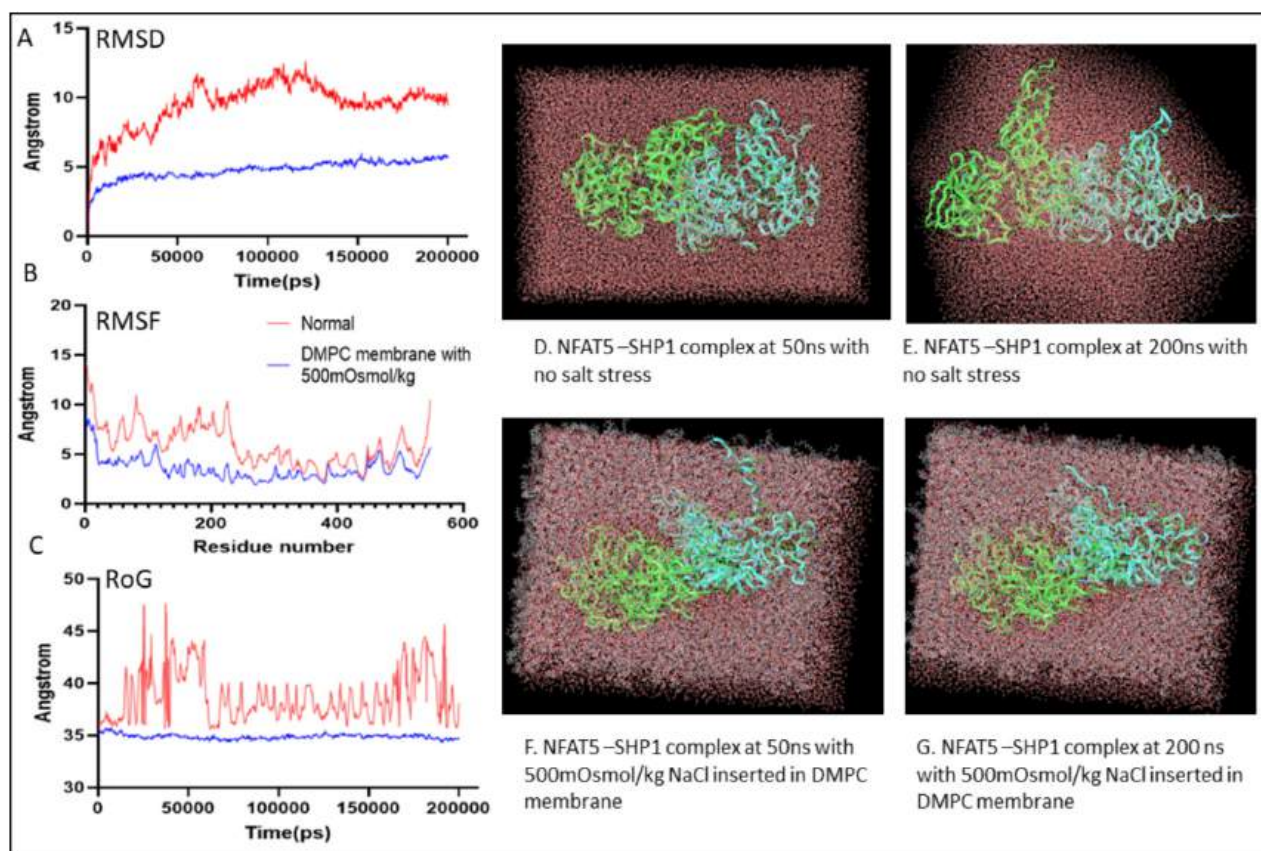
Fig. 2. Analysis of truncated SHP-1 (Cyan) and AED_DBD_NFAT5 (Green) docked complex in hypertonic condition embedded in DMPC membrane. (A) RMSD (B) RMSF (C) RoG (D-E) Conformation of complex in normal osmotic conditions at 50 ns and 200 ns. (F-G) Conformation of complex in hypertonic conditions in DMPC membrane at 50 ns and 200 ns. (For interpretation of the references to colour in this figure legend, the reader is referred to the web version of this article.)

The complex was observed to interact and maintain their conformational folds throughout the simulation (Fig. 2 D-2G).

L.major infection induces immune response in peritoneal macrophages by not only inducing the expression of pro-inflammatory cytokines but also through promotion of parasite survival response in these cells [21,22]. Depending on the infection and infection with HSD condition, activation of macrophage phenotype may identify state-of the art phenotype induced in the macrophages which may decipher the type of immune response that is elucidated in host. NFAT5 and SHP-1 complex was observed to be stable in hypertonic environment, therefore we further validated their localization expression pertaining in peritoneal macrophages and if localization of SHP-1 in nucleus might have an inhibitory effect on translocation of NFAT5 to nucleus. (Fig. 3A and S1) shows NFAT5 localized expression in peritoneal macrophages is significantly high as compared to peritoneal macrophages isolated from control and infected experimental mice groups. (Fig. 3A and S1) further shows, SHP-1 localized expression in peritoneal macrophages isolated from HSD group is significantly lower and that in peritoneal macrophages isolated from infected group is higher. In Fig. 3B, we might observe increase in NFAT5 localization in nucleus in peritoneal macrophages isolated from HSD mice as compared to localization prevalent in peritoneal macrophages of control and infected. On the contrary, SHP-1 localization might be more prominent near nucleus of peritoneal macrophages isolated from infected mice and is lower inside the nucleus of peritoneal macrophages isolated from HSD mice (Fig. 3C).

As the complex was stable in hypertonic condition in DMPC membrane embedded environment, we may suggest that in CL lesion, truncated SHP-1 may inhibit NFAT5 translocation to nucleus at nuclear membrane as well. Hence, to obstruct this interaction and to promote nuclear translocation of NFAT5 to activate IL-12 and inhibit IL-10, we

had designed inhibitory peptides and had reported their physico-chemical, structural, evolutionary parameters and identified interacting residues [10]. To study if these peptides can interact with SHP-1 we simulated docked complexes of PepA-SHP1, PepB-SHP1, and PepC-SHP1 in normal conditions and PepA-SHP1 in hypertonic condition for 200 ns. TPI1 an inhibitor of SHP-1, was used as the reference [23].

Fig. 4 shows interaction of truncated SHP-1 with PepA, PepB, and PepC in normal osmotic conditions (S2 and S3) and interaction of SHP-1 with PepA in hypertonic condition post 200 ns simulation (Fig. 4A-4D). RMSD highlighted PepA and truncated SHP-1 interaction to be more stable than PepB and PepC, therefore PepA-SHP1 complex was simulated in hypertonic conditions and it revealed RMSD of 10 Å with minor fluctuations between 5 and 9 Å (Fig. 4E). Low fluctuations were observed at all residues in PepA-SHP1 complex in hypertonic conditions with high fluctuations in RoG from 50 ns (Fig. 4F and G). Ligand RMSD (right Y-axis) highlighted that the ligand is stable with respect to the protein and its binding domain (Fig. 4H). The interaction fraction was higher (>1) at phosphatase catalytic domain of truncated SHP-1 suggesting the interactions and contacts between PepA and catalytic domain containing amino acids were stable throughout the simulation and the stability was achieved by forming water bridges, hydrogen bonds, ionic interactions and hydrophobic bonds (Fig. 4I). Formation intraHB within the ligand was also observed. The PepA was also accessible by water in hypertonic conditions which was revealed through SASA plot and PSA highlighted the contribution of nitrogen and oxygen groups in PepA towards Solvent accessible surface area (Fig. 4J). SHP-1 TPI1 complex RMSD was stable with high fluctuations in RMSF and RoG (S4). Interaction analysis of TPI1 with SHP-1 in hypertonic state revealed lower interaction fraction towards SHP-1 at C-terminal phosphatase domain as compared to PepA (S5).
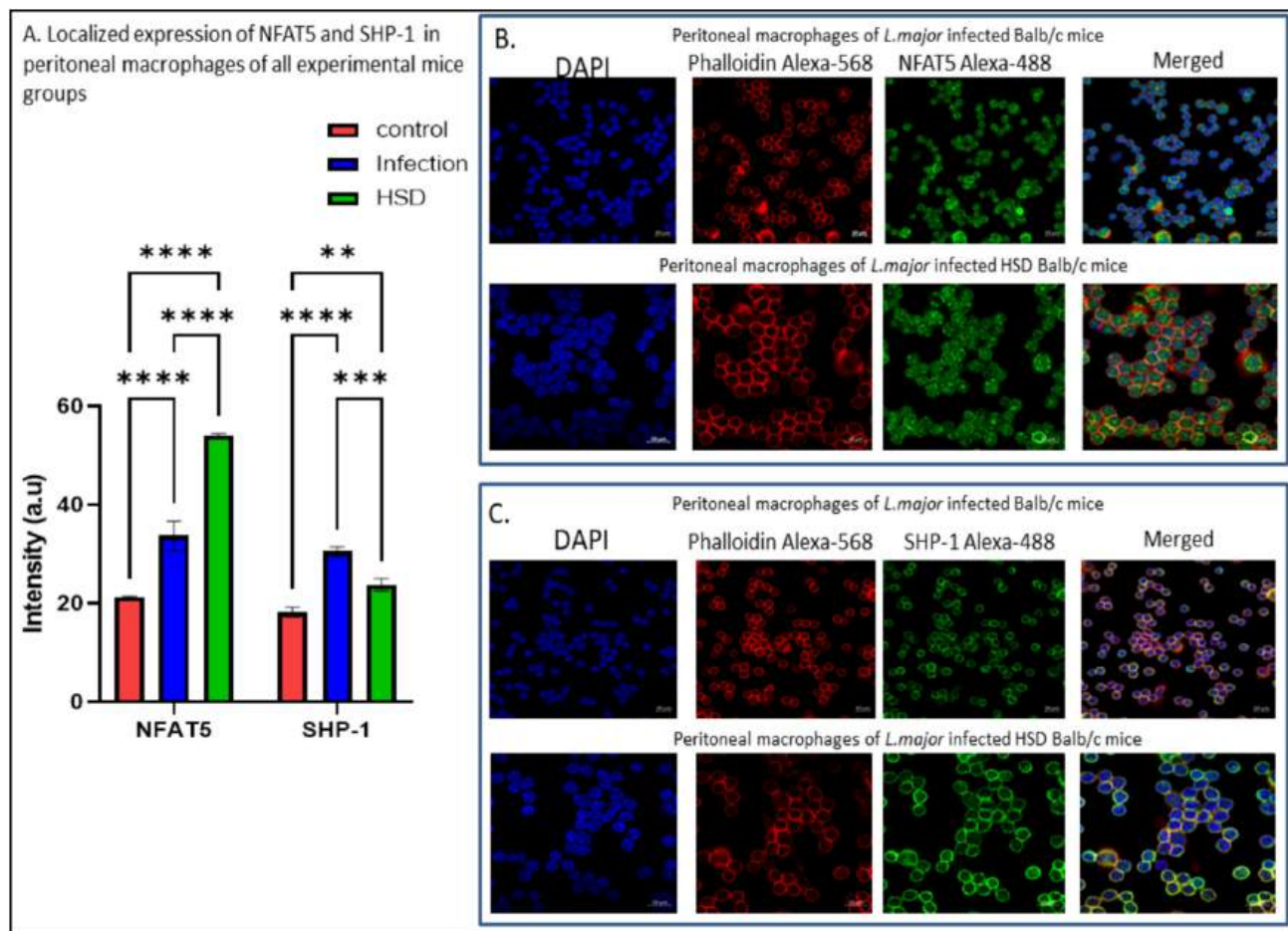
Fig. 3. (A) Measurement of fluorescence intensity of NFAT5 and SHP-1 in peritoneal macrophages of all experimental groups (Two-way ANOVA and Bonferroni correction (p-value <0.0001)) (B) Localized expression of NFAT5 in peritoneal macrophages of infected and HSD mice (C) Localized expression of SHP-1 in peritoneal macrophages of infected and HSD mice.

For peptide delivery in cellular environment, peptides should possess cell penetrating property and should show transient stable interactions with plasma membrane [24]. Hence, we simulated peptides in Cholesterol anchored DMPC membrane in hypertonic condition. We observed PepA to be more stable than PepB and PepC for 200 ns (Fig. 5 A). Amino acids at their respective position showed low atomic fluctuations (Fig. 5B). We also observed PepA made contacts with cholesterol between 100 and 200 ns (Fig. 5C). (Fig. 5 D, E and F) shows image of PepA, PepB, PepC structures embedded in cholesterol anchored DMPC membrane at 500mOsmol/kg osmotic stress at 200 ns which indicates stability of system was higher with PepA. (Fig. 5 G, H and I) indicates the amino acid in PepA, PepB and PepC that are interacting with cholesterol and predominantly though hydrophobic interactions, hydrogen bonds and water bridges. Higher interaction fraction was observed between PepA and cholesterol. PepA was also localized in cytoplasmic fraction which had TIP3P with 500mOsmol/kg hypertonicity post 200 ns simulation (Fig. 5D and G). We assume that PepA may have migrated from hydrophobic environment to hydrophilic due to its hydropathy index.

The host response to CL induced by *L.major* was examined in both infected and HSD mice groups. Notably, there was no significant difference in the weight of mice in the HSD group (Fig. 6A). However, a marked reduction in lesion size was identified in the infected HSD group compared to other groups (Fig. 6B). Analysis of NFAT5 expression in peritoneal macrophages revealed higher levels in the HSD group compared to the other groups (Fig. 6C). Furthermore, the cutaneous lesions in HSD mice exhibited an intact skin barrier, reduced immune cell infiltration, and smaller vacuole sizes compared to the infected

group (Fig. 6D). Interestingly, the lesions in HSD mice showed increased NFAT5 expression and decreased SHP-1 expression, in contrast to the infected group, which exhibited high SHP-1 and low NFAT5 expression (Fig. 6E). These findings suggest distinct immunological responses and skin barrier characteristics in HSD mice during *L.major*-induced CL.

To investigate the inflammatory response to infection in both infected and HSD mice, we employed FACS to identify M1 and M2 macrophages expressing CD80 and CD163 cell surface markers, respectively, in the context of CL [25]. Our observations revealed a significant decrease in CD80 positive (CD80+) population and increase in CD163 positive (CD163+) population in infected mice lesion (Fig. 7A). Conversely, the CD80+ population was higher in HSD mice and CD163+ cell population was notably lower in the HSD group compared to infected mice (Fig. 7B and C). Additionally, nitrite level estimation, serving as an indicator of NO in the sera, indicated that HSD mice may exhibit elevated NO levels compared to the control and infection groups (Fig. 7D). Furthermore, cytokine levels of IL-12 and IL-10 were assessed using ELISA. Notably, IL-12 levels were significantly lowest in the infected mice group, whereas HSD mice exhibited a higher concentration of IL-12 (Fig. 7E). Results showed lower levels of IL-10 in HSD mice compared to other experimental groups, with the infection group displaying a higher concentration of IL-10 (Fig. 7F). These findings shed light on the immune responses and cytokine profiles in the context of CL.
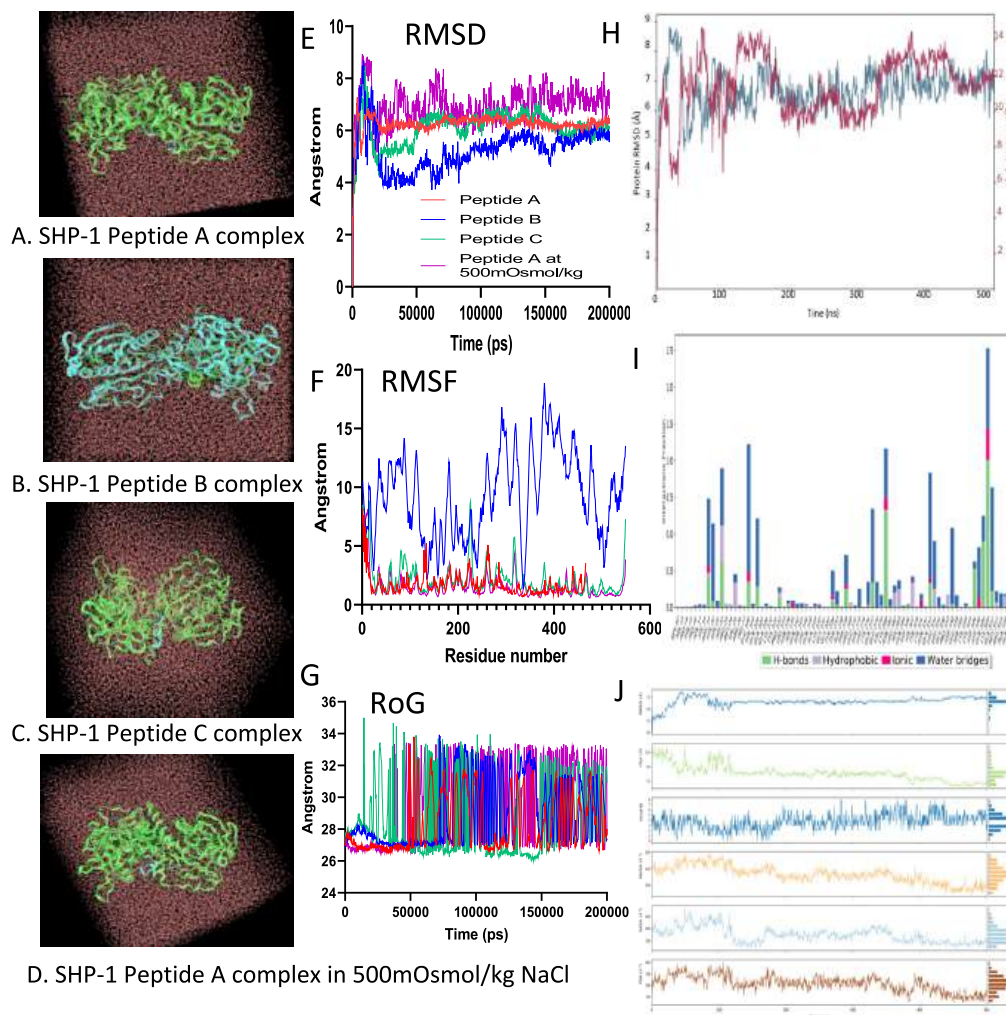
Fig. 4. (A-C) Interaction of PepA (Cyan), PepB (Green), PepC (Cyan) with truncated SHP-1 in normal osmolality. (D) Interaction of PepA (Cyan) in hypertonic condition with truncated SHP-1. (*E*-G) RMSD, RMSF and RoG of peptides with truncated SHP-1 (H) truncated SHP-1 and PepA RMSD in hypertonic condition (I) Interaction fraction of PepA with truncated SHP-1 in hypertonic condition (J) Ligand property plot of PepA with truncated SHP-1 in hypertonic condition. (For interpretation of the references to colour in this figure legend, the reader is referred to the web version of this article.)

4. Discussion

In *L.major* infection Na + accumulation has been reported to be predominant in skin lesions leading to immune cell mediated hypertonic microenvironment. This activates macrophages to upregulate NFAT5 through p38 mitogen-activated protein kinases, which produces NOS2 and promotes parasite elimination. The advantage of Na + accumulation is still unknown although its metabolism is predicted to be associated with strengthening skin barrier [26]. Hence, to understand the molecular interactions underlying the hypertonic environment we performed MDS and attempted to mimic the hypertonic environment.

NFAT5 protein consists of Transcription activation domain, DNA binding domain and Regulatory domain and SHP-1 has SH1, SH2 and phosphatase domain. To analyze NFAT5 and SHP-1 atomic stability in hypertonic state we employed NFAT5 structure which had Transcription activation domain and DNA binding domain to reduce the bulkiness of system. Truncated SHP-1 may be the virulent form which may persist in cutaneous lesion, as lipid rafts mediates the GP63 access to SHP-1 upon parasite internalization [18]. Later, SHP-1 may inhibit NFAT5 and promote Extracellular signal-regulated kinase mediated IL-10 synthesis [27].

The simulation of NFAT5 and SHP-1 in hypertonic conditions displayed stable molecular motions. SHP-1 inhibiting NFAT5 at nuclear membrane is also prevalent prospect; therefore with hypertonicity we additionally embedded the structure in DMPC membrane as this membrane in particular is close to mammalian membrane [28] [29]. Their interactions were also relatively stable in hypertonic environment. SHP-1 upon getting truncated by GP63 localizes to nuclear envelope putting it close to its target transcription factor [30]. Knocking down SHP-1 was reported to upregulate NFAT5 transcriptional activity in *L.donovani* infected HEK293 cells in hypertonic condition both *in vitro* and *in vivo*. Association of SHP-1 and NFAT5 interaction in hypertonic condition was decreased as co-immunoprecipitation of both proteins was affected [31]. These findings suggested that SHP-1 physically interacts with NFAT5 in *Leishmania* infected condition to inhibit NFAT5 translocation inside nucleus. Our findings from confocal studies of NFAT5 and SHP-1 localized expression in all experimental groups suggested that SHP-1 expression inside nucleus was significantly lower in peritoneal macrophages isolated from HSD mice group whereas NFAT5 expression was significantly higher in peritoneal macrophages isolated from HSD mice which may suggest that NFAT5 transcriptional activity will be more prominent in the cells of this group which might be associated with high pro-inflammatory response and develop parasite eliminating effect. As, peritoneal macrophage isolated from infected group showed low expression in nucleus it is essential to inhibit the SHP-1 to enable NFAT5 translocation to nucleus.
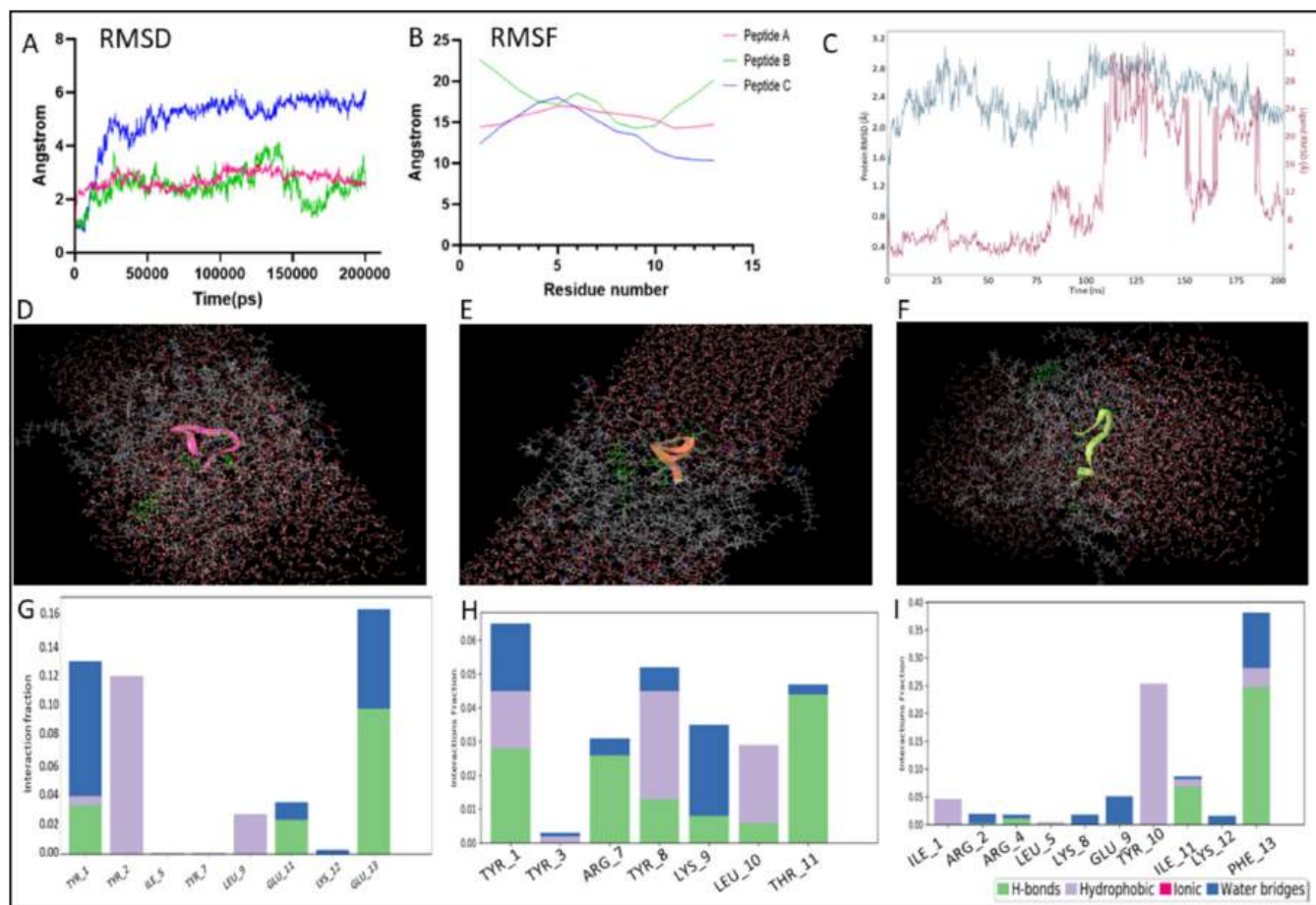
Fig. 5. Simulation of peptides in cholesterol anchored DMPC membrane in hypertonic state. (A and B) RMSD and RMSF of PepA (pink), PepB (orange) and PepC (green). C. RMSD plot of PepA and cholesterol. (D—F) Images of PepA, PepB and PepC post simulation at 200 ns. (G-I) Interaction plots of PepA, PepB and PepC with cholesterol. (For interpretation of the references to colour in this figure legend, the reader is referred to the web version of this article.)

As peptides have a high affinity and specificity for binding protein surfaces, they have demonstrated potential as modulators of protein–protein interactions. Numerous peptides have received FDA approval and are being developed as immunosuppressant and antibiotics; many more are still in various phases of development [32]. MDS developed a method for predicting protein-peptide interaction with respect to their conformations during association [33]. It is also a pipeline which is developed to understand if a peptide can permeate a membrane by analyzing the trajectories of MDS [34]. Therefore we analyzed the interactions of SHP-1 and peptide complex and PepA in hypertonic condition showed better interaction stability with SHP-1. PepA also depicted stability in DMPC membrane anchored with cholesterol the orientation of peptide was observed to be dynamic in hypertonic condition.

To overcome the barriers of peptide delivery such as biodegradation/metabolism, albumin binding and aggregation, insolubility, low permeability *via* vascular endothelial cell layers, rapid elimination by the kidney, and ineffective cellular internalization, a novel drug delivery system is needed to enhance cell membrane penetration properties [35]. Hence, these peptides may be delivered using methods which involve liposomal entrapment and delivery, nanoparticles mediated delivery, drug conjugated delivery, antibody conjugated delivery or in the form of synthetic circuit.

In both mice and humans subjected to a HSD, there is observed sodium accumulation at localized tissue-sensitive sites, leading to an enrichment of inflammatory macrophages in specific areas, particularly in lesions of CL models [7]. Previous studies have noted that HSD-fed mice experience weight loss when provided with 4% NaCl in their diet

[36]. In our study, we developed a model utilizing 1% NaCl in drinking water, which did not significantly impact the weight of mice. The lesions in HSD mice were notably smaller compared to infected mice, and this correlated with higher levels of NFAT5, known to regulate hypertonicity, activate iNOS and IL-12 signaling while inhibiting IL-10 signaling [9]. We investigated expression levels of NFAT5 in peritoneal macrophages of all experimental models which revealed that NFAT5 levels were higher in HSD mice as compared to other groups. Histopathology reports of lesion shows the skin barrier strengthens of HSD mice whereas skin barrier of infected group is compromised [37] which corroborate with our findings. Immune cell population which includes macrophages, neutrophils, dendritic cells and T-cells has been identified in ear lesion [38,39] which signifies our findings from histopathology data as we also observed immune cells to be present in lesion of experimental groups. Skin biopsies of patients with CL revealed the presence of vacuoles containing amastigotes with inflammatory patterns [40] which we observed in infected and HSD mice ear lesion where, vacuoles size of HSD mice was smaller than infected mice vacuoles. Impact of infection of NFAT5 and SHP-1 expression in lesion of infected and HSD mice was studied as they have been reported as cross talk points from our previous findings and peptides have been designed against SHP-1 to obtain parasite eliminating effect [9,10]. From immuno-histochemistry analysis, SHP-1 expression was reduced in HSD mice and expression of NFAT5 was higher which goes in is accord with our findings. Hence, we assumed that the HSD mice which we developed had non-significant impact on mice weight by also upregulating NFAT5 an indicator of hypertonicity and crosstalk point and lower parasite load.

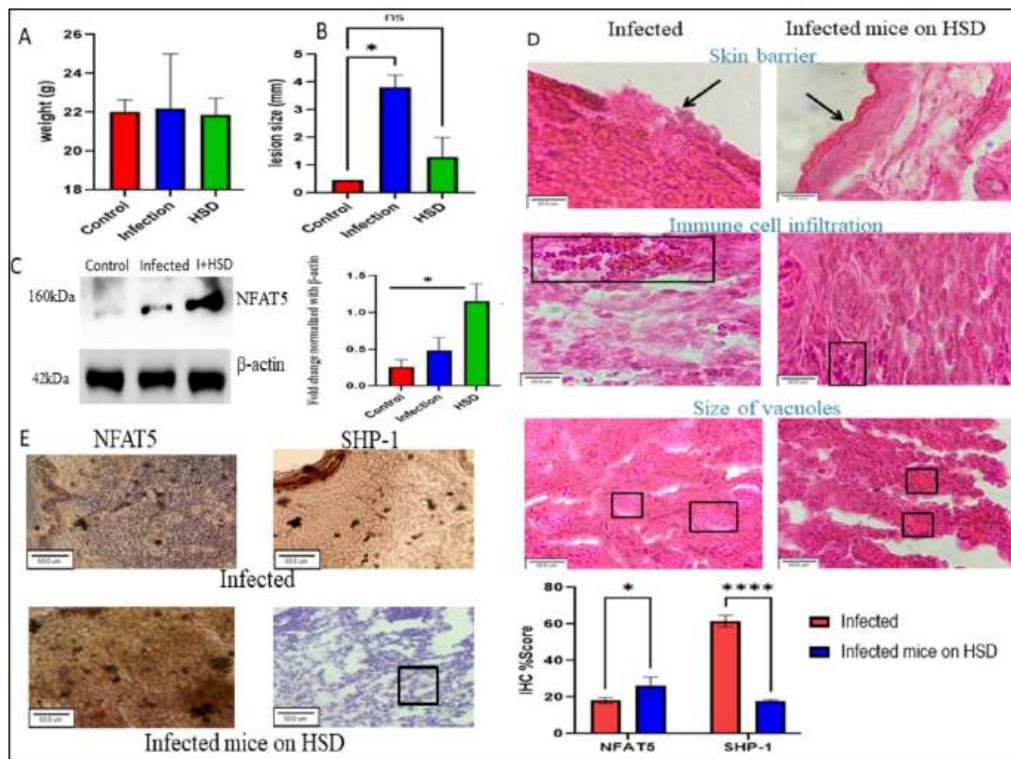To comprehend the host immune response to infection, we assessed

Fig. 6. Effect of HSD on NFAT5 and SHP-1 expression in lesion. (A) Analysis of difference in weights of experimental mice groups (*p*-value = ns) (B) Difference in lesion size of experimental mice (One way ANOVA (p-value<0.05)) (C) NFAT5 expression in peritoneal macrophages of experimental groups with densitometry analysis (One way ANOVA (p-value<0.05) (D) Histopathological staining using H&E stains for lesions of infected and HSD mice (E) Immuno-histochemistry of NFAT5 and SHP-1 in lesions of infected and HSD mice (Two- way ANOVA with Bonferroni's correction (p-value<0.05)).

all experimental groups on the basis of the macrophage population enrichment, NO levels present in sera and cytokine profile. For FACS studies, CD80+ cells were classified as M1 macrophages and CD163+ cells were classified as M2 macrophage as they have been widely used for sorting M1/M2 phenotype [41,42]. CD80+ M1 cells induces pro-inflammatory response producing cytokine like IL-12 and induce NO for parasite elimination [43] whereas, M2 cells induces anti-inflammatory response and produce cytokine like IL-10 which inhibits NO and lead to parasite proliferation [44]. Our results indicate that HSD mice had higher parasite eliminating response as the group had higher number of CD80+ cells and lower CD163+ cells which also validate our findings from immunoblotting, histopathology and immuno-histochemistry data that HSD may induce parasite eliminating response where NFAT5 is upregulated and SHP-1 is downregulated. On the contrary, infected group had high CD163+ cells and lower CD80+ cells indicative of parasite proliferating response where we observed high SHP-1 expression and low NFAT5 expression. NO is the direct measure of identifying parasite eliminating response [45], HSD group depicted high NO levels as compared to infection group suggesting high pro-inflammatory response and depletion in parasite load in lesion. IL-10 and IL-12 have reported by us that they have a reciprocal axis which is controlled by NFAT5 and SHP-1 for which, we have developed peptides using artificial intelligence and machine learning approaches to upregulate IL-12 and down regulate IL-10 to obtain parasite eliminating effect [9] [10]. ELISA of IL-10 and IL-12 highlight that HSD mice have higher pro-inflammatory cytokine levels and lower anti-inflammatory cytokine concentration which might play an essential role in parasite elimination.

factor regulation, protein-protein interaction regulation through peptides, protein-peptide stability and stability of peptide in membrane. We studied the molecular dynamics of NFAT5 and SHP-1 atomic motions and evaluated their interaction complex's stability. Inhibitory peptides which were designed to inhibit phosphatase catalytic active residues of truncated SHP-1 were evaluated for their interactions with SHP-1 and their stability in DMPC membrane. Peptide A may be chosen as a potential peptide to evaluate its property to promote parasite elimination. We developed HSD mice model and underlined the effect of NFAT5 expression and SHP-1 downregulation on lesion size as well as on parasite load in the lesion. We deciphered the effect of infection and HSD on cellular localization of NFAT5 and SHP-1 and analyzed the effect of infection and HSD on nuclear translocation dependent NFAT5 transcriptional activity. We also outlined the immunological aspect with respect to parasite eliminating and parasite survival response by characterizing the percentage of M1 and M2 population present in lesion. We estimated the levels of NO produced in mice which may combat the parasite by inhibiting their growth and proliferation. IL-10 and IL-12 levels indicated that the cytokine paradigm is shifted to pro-inflammatory cytokine side in HSD mice. Further, we aim to deliver the peptide, for which we may adopt synthetic biology approach. The peptide sequence can be inserted in an inducible fashion in an operon based model with plasmid backbone and delivered to the cells by transfection. In future, we may evaluate the PepA for SHP-1 binding *in vitro* and evaluate parasite elimination *in vitro* as well as in parasite challenged mice model. This model may be used for other disease models pertaining to infection and inflammation where a protein is a potential target and peptide is the choice of therapeutic.

5. Conclusion

Through our work we mimicked the hypertonic environment that is predominant in CL lesion. We presented MDS models for transcription

Animal ethics

All animal experiments conducted in this study were ethically approved by the Institutional Animal Ethics Committee (IAEC) of the
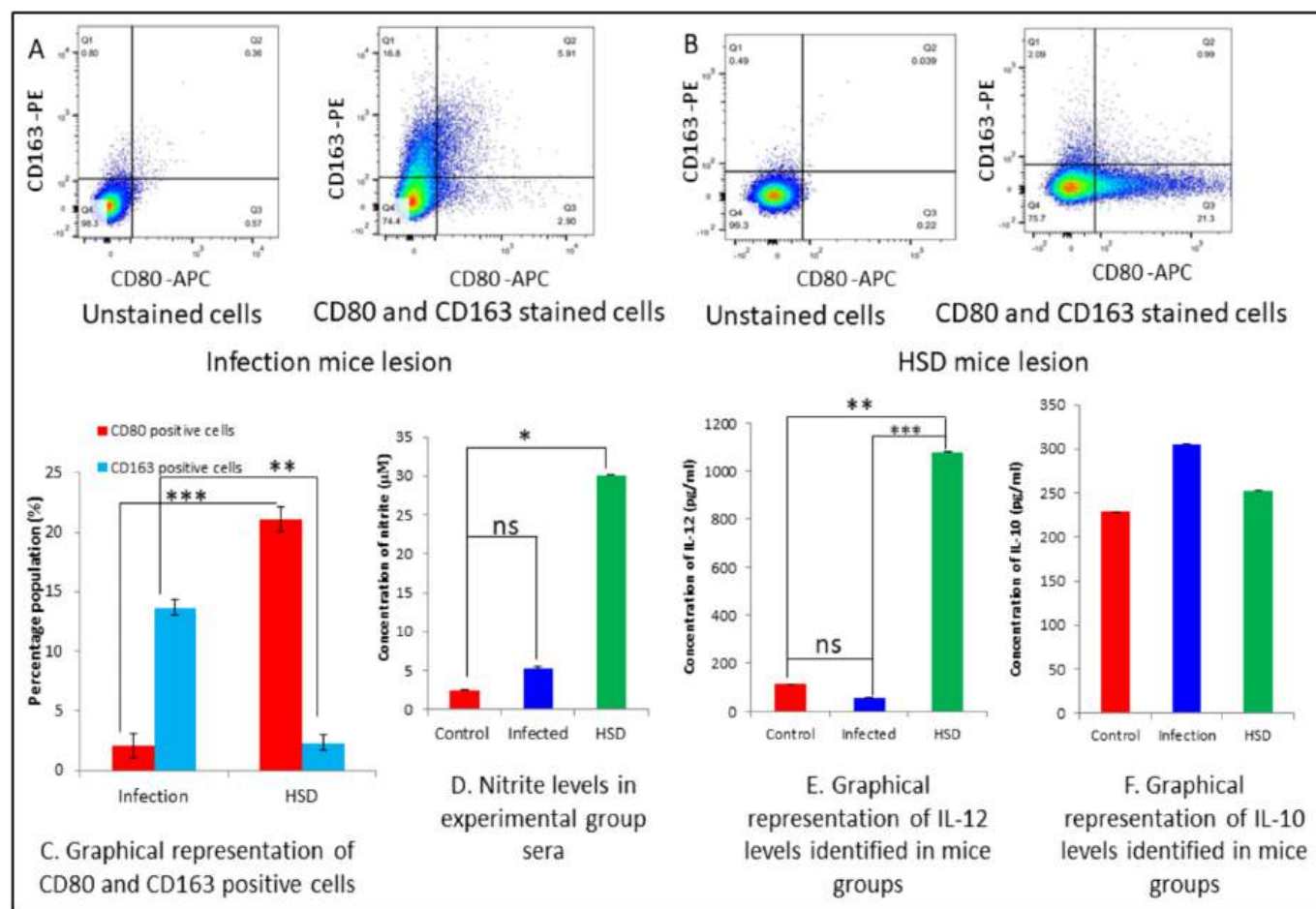
Fig. 7. Analysis of immune response to *L.major* infection in all experimental groups. (A) FACS analysis of M1/M2 macrophages in infected lesions (B) FACS analysis of M1/M2 macrophages in HSD lesions (C) Graphical representation of percentage population of M1 and M2 phenotypes (students *t*-test (*p*-value<0.01 and 0.001)) Mean absorbance levels were measured at 95% confidence interval (CI). (D) Concentration of NO estimated in sera of all groups (One way ANOVA (p-value<0.05)). (E) Estimated concentration of IL-12 in sera of all experimental groups (One way ANOVA (p-value<0.01 and 0.001)). (F) Estimated concentration of IL-10 in sera of all experimental groups (One way ANOVA p-value = ns).

CRediT authorship contribution statement

Shweta Khandibharad: Writing – review & editing, Writing – original draft, Visualization, Validation, Software, Resources, Methodology, Investigation, Formal analysis, Data curation. **Shailza Singh:** Writing – review & editing, Supervision, Software, Resources, Project administration, Methodology, Investigation, Funding acquisition, Formal analysis, Conceptualization.

Declaration of competing interest

The authors potentially declare no conflict of interest.

Data availability

No data was used for the research described in the article.

Acknowledgements

Appendix A. Supplementary data

Supplementary data to this article can be found online at https://doi.org/10.1016/j.bbagen.2024.130670.

References

[1] G. Sliwoski, S. Kothiwale, J. Meiler, E.W.J. Lowe, Computational methods in drug discovery, Pharmacol. Rev. 66 (2014) 334–395.
[2] D.B. Singh, Success, limitation and future of computer aided drug designing, Transl Med (2014) 04.
[3] R. Wadhwa, N.S. Yadav, S.P. Katiyar, T. Yaguchi, C. Lee, H. Ahn, C.-O. Yun, S. C. Kaul, D. Sundar, Molecular dynamics simulations and experimental studies reveal differential permeability of withaferin-a and withanone across the model cell membrane, Sci. Rep. 11 (2021) 2352.
[4] R.W. Benz, F. Castro-Román, D.J. Tobias, S.H. White, Experimental validation of molecular dynamics simulations of lipid bilayers: a new approach, Biophys. J. 88 (2005) 805–817.
[5] K.E. Sharquie, A new intralesional therapy of cutaneous leishmaniasis with hypertonic sodium chloride solution, J. Dermatol. 22 (1995) 732–737.
[6] M. Wang, High-salt diet aggravates pyelonephritis, Nat. Rev. Nephrol. 16 (2020) 315.
[7] K. Jobin, D.N. Müller, J. Jantsch, C. Kurts, Sodium and its manifold impact on our immune system, Trends Immunol. 42 (2021) 469–479.
[8] J. Aramburu, C. López-Rodríguez, Regulation of inflammatory functions of macrophages and T lymphocytes by NFAT5, Front. Immunol. 10 (2019) 535.

[9] S. Khandibharad, S. Singh, Computational system level approaches for discerning reciprocal regulation of IL10 and IL12 in Leishmaniasis, Front. Genet. 12 (2022) 1–14.

[10] S. Khandibharad, S. Singh, Artificial intelligence channelizing protein-peptide interactions pipeline for host-parasite paradigm in IL-10 and IL-12 reciprocity by SHP-1, Biochim. Biophys. Acta Mol. basis Dis. 1868 (2022) 166466.

[11] N. Samarth, R. Kabra, S. Singh, Anthraquinolone and quinolizine derivatives as an alley of future treatment for COVID-19: an in silico machine learning hypothesis, Sci. Rep. 11 (2021) 17915.

[12] I. Syuhada, N.U.J. Hauwali, A. Rosikhin, E. Sustini, F.A. Noor, T. Winata, Bond order redefinition needed to reduce inherent noise in molecular dynamics simulations, Sci. Rep. 11 (2021) 3674.

[13] P. Kunzmann, J.M. Anter, K. Hamacher, Adding hydrogen atoms to molecular models via fragment superimposition, Algorithms. Mol. Biol. 17 (2022) 7.

[14] M.C. Childers, V. Daggett, Insights from molecular dynamics simulations for computational protein design, Mol. Syst. Des. Eng. 2 (2017) 9–33.

[15] G. Surmeier, M. Paulus, P. Salmen, S. Dogan, C. Sternemann, J. Nase, Cholesterol modulates the pressure response of DMPC membranes, Biophys. Chem. 252 (2019) 106210.

[16] K.J. Bowers, E. Chow, H. Xu, R.O. Dror, M.P. Eastwood, B.A. Gregersen, J. L. Klepeis, I. Kolossvary, M.A. Moraes, F.D. Sacerdoti, J.K. Salmon, Y. Shan, D. E. Shaw, Scalable algorithms for molecular dynamics simulations on commodity clusters, in: proceedings of the 2006 ACM/IEEE Conference on Supercomputing, Association for Computing Machinery, New York, NY, USA, 2006, 84–es.

[17] M. Olivier, V.D. Atayde, A. Isnard, K. Hassani, M.T. Shio, Leishmania virulence factors: focus on the metalloprotease GP63, Microbes Infect. 14 (2012) 1377–1389.

[18] M.A. Gomez, I. Contreras, M. Hallé, M.L. Tremblay, R.W. McMaster, M. Olivier, Leishmania GP63 alters host signaling through cleavage-activated protein tyrosine phosphatases, Sci. Signal. 2 (2009) ra58.

[19] H. Seeger, D. Kitterer, J. Latus, M.D. Alscher, N. Braun, S. Segerer, The potential role of NFAT5 and osmolarity in peritoneal injury, Biomed. Res. Int. 2015 (2015) 578453.

[20] X. Zhou, M. Gallazzini, M.B. Burg, J.D. Ferraris, Contribution of SHP-1 protein tyrosine phosphatase to osmotic regulation of the transcription factor TonEBP/OREBP, Proc. Natl. Acad. Sci. USA 107 (2010) 7072–7077.

[21] A.A. Filardy, A.C. Costa-da-Silva, C.M. Koeller, K. Guimarães-Pinto, F.L. Ribeiro-Gomes, M.F. Lopes, N. Heise, C.G. Freire-de-Lima, M.P. Nunes, G.A. DosReis, Infection with Leishmania major induces a cellular stress response in macrophages, PLoS One 9 (2014) e85715.

[22] A.C. Costa-da-silva, D.D.O. Nascimento, J.R.M. Ferreira, K. Guimar, L. Freire-de-lima, A. Morrot, D. Decote-ricardo, A.A. Filardy, C.G. Freire-de-lima, Immune Responses in Leishmaniasis : An Overview, 2022, pp. 1–16.

[23] S. Kundu, K. Fan, M. Cao, D.J. Lindner, Z.J. Zhao, E. Borden, T. Yi, Novel SHP-1 inhibitors tyrosine phosphatase inhibitor-1 and analogs with preclinical anti-tumor activities as tolerated oral agents, J. Immunol. 184 (2010) 6529–6536.

[24] Z. Guo, H. Peng, J. Kang, D. Sun, Cell-penetrating peptides: possible transduction mechanisms and therapeutic applications, Biomed. Report. 4 (2016) 528–534.

[25] H. Wijesooriya, N. Samaranayake, N.D. Karunaweera, Cytokine and phenotypic cell profiles in human cutaneous leishmaniasis caused by Leishmania donovani, PLoS One 18 (2023) e0270722.

[26] J. Jantsch, V. Schatz, D. Friedrich, A. Schröder, C. Kopp, I. Siegert, A. Maronna, D. Wendelborn, P. Linz, K.J. Binger, M. Gebhardt, M. Heinig, P. Neubert, F. Fischer, S. Teufel, J.-P. David, C. Neufert, A. Cavallaro, N. Rakova, C. Küper, F.-X. Beck, W. Neuhofer, D.N. Muller, G. Schuler, M. Uder, C. Bogdan, F.C. Luft, J. Titze, Cutaneous Na+ storage strengthens the antimicrobial barrier function of the skin and boosts macrophage-driven host defense, Cell Metab. 21 (2015) 493–501.

[27] T.H. Khan, N. Srivastava, A. Srivastava, A. Sareen, R.K. Mathur, A.G. Chande, K. V. Musti, S. Roy, R. Mukhopadhyaya, B. Saha, SHP-1 plays a crucial role in CD40 signaling reciprocity, J. Immunol. 193 (2014) 3644–3653.

[28] A. Luchini, G. Vitiello, Mimicking the mammalian plasma membrane: an overview of lipid membrane models for biophysical studies, Biomimetics (Basel, Switzerland) 6 (2020).

[29] P. Jurczak, K. Szutkowski, S. Lach, S. Jurga, P. Czaplewska, A. Szymanska, I. Zhukov, DMPC phospholipid bilayer as a potential Interface for human cystatin C oligomerization: analysis of protein-liposome interactions using NMR spectroscopy, Membranes (Basel) 11 (2020).

[30] A. Isnard, M.T. Shio, M. Olivier, Impact of Leishmania metalloprotease GP63 on macrophage signaling, Front. Cell. Infect. Microbiol. 2 (2012) 72.

[31] X. Zhou, H. Wang, N.L. Koles, A. Zhang, N.E. Aronson, Leishmania infantum-chagasi activates SHP-1 and reduces NFAT5/TonEBP activity in the mouse kidney inner medulla, Am. J. Physiol. Ren. Physiol. 307 (2014) F516–F524.

[32] J. Damjanovic, J. Miao, H. Huang, Y.-S. Lin, Elucidating solution structures of cyclic peptides using molecular dynamics simulations, Chem. Rev. 121 (2021) 2292–2324.

[33] J. Wang, A. Alekseenko, D. Kozakov, Y. Miao, Improved modeling of peptide-protein binding through global docking and accelerated molecular dynamics simulations, Front. Mol. Biosci. 6 (2019) 112.

[34] D.P. Tran, S. Tada, A. Yumoto, A. Kitao, Y. Ito, T. Uzawa, K. Tsuda, Using molecular dynamics simulations to prioritize and understand AI-generated cell penetrating peptides, Sci. Rep. 11 (2021) 10630.

[35] D. Berillo, A. Yeskendir, Z. Zharkinbekov, K. Raziyeva, A. Saparov, Peptide-based drug delivery systems, Medicina (Kaunas) 57 (2021).

[36] S.L.F. Aguiar, M.C.G. Miranda, M.A.F. Guimarães, H.C. Santiago, C.P. Queiroz, P. S. da Cunha, D.C. Cara, G. Foureaux, A.J. Ferreira, V.N. Cardoso, P.A. Barros, T. U. Maioli, A.M.C. Faria, High-salt diet induces IL-17-dependent gut inflammation and exacerbates colitis in mice, Front. Immunol. 8 (2017) 1969.

[37] M.M. Eissa, E.I. Amer, S.F. Mossallam, M.M. Gomaa, N.M. Baddour, Miltefosine for Old World cutaneous leishmaniasis: an experimental study on Leishmania major infected mice, Alexandria J. Med. 48 (2012) 261–271.

[38] G. Venugopal, J.T. Bird, C.L. Washam, H. Roys, A. Bowlin, S.D. Byrum, T. Weinkopff, In vivo transcriptional analysis of mice infected with Leishmania major unveils cellular heterogeneity and altered transcriptomic profiling at single-cell resolution, PLoS Negl. Trop. Dis. 16 (2022) e0010518.

[39] H. Wijesinghe, N. Gunathilaka, S. Semege, N. Pathirana, N. Manamperi, C. de Silva, D. Fernando, Histopathology of cutaneous Leishmaniasis caused by Leishmania donovani in Sri Lanka, Biomed. Res. Int. 2020 (2020) 4926819.

[40] K. González, R. Diaz, A.F. Ferreira, V. García, H. Paz, J.E. Calzada, M. Ruíz, M. Laurenti, A. Saldaña, Histopathological characteristics of cutaneous lesions caused by Leishmania Viannia panamensis in Panama, Rev. Inst. Med. Trop. Sao Paulo 60 (2018) e8.

[41] F.R. Bertani, P. Mozetic, M. Fioramonti, M. Iuliani, G. Ribelli, F. Pantano, D. Santini, G. Tonini, M. Trombetta, L. Businaro, S. Selci, A. Rainer, Classification of M1/M2-polarized human macrophages by label-free hyperspectral reflectance confocal microscopy and multivariate analysis, Sci. Rep. 7 (2017) 8965.

[42] C.M. Sandoval Pacheco, G.V. Araujo Flores, K. Gonzalez, C.M. de Castro Gomes, L. F.D. Passero, T.Y. Tomokane, W. Sosa-Ochoa, C. Zúniga, J. Calzada, A. Saldaña, C. E.P. Corbett, F.T. Silveira, M.D. Laurenti, Macrophage polarization in the skin lesion caused by Neotropical species of Leishmania sp, J Immunol Res 2021 (2021) 5596876.

[43] F. Raggi, S. Pelassa, D. Pierobon, F. Penco, M. Gattorno, F. Novelli, A. Eva, L. Varesio, M. Giovarelli, M.C. Bosco, Regulation of human macrophage M1-M2 polarization balance by hypoxia and the triggering receptor expressed on myeloid Cells-1, Front. Immunol. 8 (2017) 1097.

[44] F. Tomiotto-Pellissier, B.T.S. da Bortoleti, J.P. Assolini, M.D. Gonçalves, A.C. M. Carloto, M.M. Miranda-Sapla, I. Conchon-Costa, J. Bordignon, W.R. Pavanelli, Macrophage polarization in Leishmaniasis: broadening horizons, Front. Immunol. 9 (2018) 2529.

[45] P. Formaglio, M. Alabdullah, A. Siokis, J. Handschuh, I. Sauerland, Y. Fu, A. Krone, P. Gintschel, J. Stettin, S. Heyde, J. Mohr, L. Philipsen, A. Schröder, P.A. Robert, G. Zhao, S. Khailaie, A. Dudeck, J. Bertrand, G.F. Späth, S. Kahlfuß, P. Bousso, B. Schraven, J. Huehn, S. Binder, M. Meyer-Hermann, A.J. Müller, Nitric oxide controls proliferation of Leishmania major by inhibiting the recruitment of permissive host cells, Immunity 54 (2021) 2724–2739.e10.